Very low Ru loadings boosting performance of Ni-based dual-function materials during the integrated CO2 capture and methanation process

Tsiotsias, Anastasios I.; Harkou, Eleana; Charisiou, Nikolaos D.; Sebastian, Victor; Naikwadi, Dhanaji R.; van der Linden, Bart; Bansode, Atul; Stoian, Dragos; Goula, Maria A.; More Authors

DOI
10.1016/j.jechem.2024.11.001

Publication date
2025

Document Version
Final published version

Published in
Journal of Energy Chemistry

Journal of Energy Chemistry 102 (2025) 309–328

Contents lists available at ScienceDirect

Journal of Energy Chemistry

journal homepage: www.elsevier.com/locate/jechem

http://www.journals.elsevier.com/journal-of-energy-chemistry/

Very low Ru loadings boosting performance of Ni-based dual-function materials during the integrated CO_2 capture and methanation process

Anastasios I. Tsiotsias [a], Eleana Harkou [b], Nikolaos D. Charisiou [a], Victor Sebastian [c,d,e], Dhanaji R. Naikwadi [f], Bart van der Linden [f], Atul Bansode [f], Dragos Stoian [g], George Manos [h], Achilleas Constantinou [b], Maria A. Goula [a,i,j,*]

[a] Laboratory of Alternative Fuels and Environmental Catalysis (LAFEC), Department of Chemical Engineering, University of Western Macedonia, Kozani 50100, Greece
[b] Department of Chemical Engineering, Cyprus University of Technology, 57 Corner of Athinon and Anexartisias, Limassol 3036, Cyprus
[c] Department of Chemical Engineering and Environmental Technology, Universidad de Zaragoza, Campus Rió Ebro-Edificio I+D, Zaragoza 50018, Spain
[d] Instituto de Nanociencia y Materiales de Aragón (INMA), Universidad de Zaragoza, CSIC, c/ Mariá de Luna 3, Zaragoza 50018, Spain
[e] Networking Research Center on Bioengineering, Biomaterials and Nanomedicine, CIBERBBN, 28029 Madrid, Spain
[f] Department of Chemical Engineering, Delft University of Technology, Van der Massweg 9, Delft 2629 HZ, the Netherlands
[g] The Swiss-Norwegian Beamlines (SNBL), European Synchrotron Radiation Facility (ESRF), Grenoble 38000, France
[h] Department of Chemical Engineering, University College London, London WCIE7JE, United Kingdom
[i] Centre for Research & Technology Hellas (CERTH), Chemical Process and Energy Resources Institute (CPERI), 52 Egialias str, Maroussi, Athens 15125, Greece
[j] School of Science and Technology, Hellenic Open University, Parodos Aristotelous 18, Patras 26335, Greece

ARTICLE INFO

Article history:
Received 14 June 2024
Revised 23 October 2024
Accepted 2 November 2024
Available online 13 November 2024

Keywords:
Dual-function materials
Integrated CO_2 capture and methanation
Bimetallic materials
Nickel-ruthenium
Reducibility
in-situ DRIFTS
CFD modelling

ABSTRACT

Herein, the effect of the Ru:Ni bimetallic composition in dual-function materials (DFMs) for the integrated CO_2 capture and methanation process (ICCU-Methanation) is systematically evaluated and combined with a thorough material characterization, as well as a mechanistic (in-situ diffuse reflectance infrared fourier-transform spectroscopy (in-situ DRIFTS)) and computational (computational fluid dynamics (CFD) modelling) investigation, in order to improve the performance of Ni-based DFMs. The bimetallic DFMs are comprised of a main Ni active metallic phase (20 wt%) and are modified with low Ru loadings in the 0.1–1 wt% range (to keep the material cost low), supported on Na_2O/Al_2O_3. It is shown that the addition of even a very low Ru loading (0.1–0.2 wt%) can drastically improve the material reducibility, exposing a significantly higher amount of surface-active metallic sites, with Ru being highly dispersed over the support and the Ni phase, while also forming some small Ru particles. This manifests in a significant enhancement in the CH_4 yield and the CH_4 production kinetics during ICCU-Methanation (which mainly proceeds via formate intermediates), with 0.2 wt% Ru addition leading to the best results. This bimetallic DFM also shows high stability and a relatively good performance under an oxidizing CO_2 capture atmosphere. The formation rate of CH_4 during hydrogenation is then further validated via CFD modelling and the developed model is subsequently applied in the prediction of the effect of other parameters, including the inlet H_2 concentration, inlet flow rate, dual-function material weight, and reactor internal diameter.

1. Introduction

The rapid rise of anthropogenic greenhouse gas emissions and concerns about climate change necessitate the development of CO_2 capture and utilization technologies (CCU) to curb the amount of CO_2 released into the atmosphere [1–3]. In the Power-to-Methane concept, CO_2 is captured from flue gases and, with the help of renewable hydrogen, is converted into synthetic natural gas (i.e., methane), that can be used to store excess renewable energy in the form of a reliable, easy-to-handle, and carbon-neutral energy carrier (Eq. (1)) [3–6]. These separate processes of CO_2 capture and then utilization via conversion to methane (i.e., methanation) can be coupled into an integrated CO_2 capture

* Corresponding author.
E-mail address: mgoula@uowm.gr (M.A. Goula).

https://doi.org/10.1016/j.jechem.2024.11.001

and methanation process (ICCU-Methanation) using "dual-function materials" (DFMs) [7–9]. During this process, CO_2 is first captured from the adsorption-active component of the DFM and is later hydrogenated into methane via the catalytically-active component [10–13].

$$CO_2 + 4H_2 \rightarrow CH_4 + 2H_2O \quad (1)$$

In the past decade, many research works have surfaced that deal with the preparation and testing of these novel dual-function materials [11,12]. It has been shown that Na_2CO_3, or "Na_2O", supported on Al_2O_3 can provide an abundance of CO_2-philic, adsorption-active sites for CO_2 capture, which is followed by spill-over and methanation on the catalytically active sites, typically comprised of Ru or Ni active metals [11,14,15]. Ru is thus far favored for this type of application due to its high reducibility, as it can easily revert back to its metallic state following oxidation during CO_2 capture under an oxidizing flue gas atmosphere [14,16]. On the other hand, Ni is a comparatively much cheaper active metal and thus, research is also directed in the preparation of Ni-based DFMs that can possess high CH_4 production capacity, fast CH_4 production kinetics, and the ability to perform the integrated cycle following oxidation and then reduction under a low operating temperature [11,17–19]. In the work of Arellano-Trevino et al. [20], it has been shown that the incorporation of 1 wt% Ru in a Ni-based DFM can promote the reducibility of the material and its performance under oxidizing CO_2 capture conditions, while Bermejo-Lopez et al. [21] reported that a bimetallic DFM with the same active metal loadings (1 wt% Ru and 10 wt% Ni) showed improved Ni dispersion, reducibility, and CH_4 production capacity compared to the Ni-based monometallic DFM.

The theoretical approach of the demonstration of the CO_2 methanation reaction is a time-saving procedure, which requires less expense and effort [22]. In this regard, computational fluid dynamics (CFD) simulations are considered as a great accomplishment, as parameters can be determined and forecast [22,23]. Transport phenomena of heterogeneous flows in reactors and key details of space-time variations in different component flows, concentrations, and temperatures are among the operational benefits that the CFD simulations offer [22–24]. The modelling of complex materials like DFMs is one of the most recent progresses in the computational field [25,26]. Bermejo-López et al. [25] proposed a kinetic model for the ICCU-Methanation process over a $Ru/Na_2CO_3/Al_2O_3$ DFM that could predict the evolution of CH_4 and precisely describe the adsorption and hydrogenation steps. Afterwards, in a subsequent study, Bermejo-López et al. [26] employed the proposed kinetic model in order to predict the temporal evolution of components at short and long adsorption and hydrogenation durations, indicating the saturation and regeneration efficiency of the material during the different steps.

A parameter that has barely been investigated in the literature dealing with DFMs for the ICCU-Methanation process is the active metal loading and/or composition in bimetallic materials. This approach is quite popular during the catalytic CO_2 methanation reaction with co-feeding of CO_2 and H_2 reactants [27–31]. For example, Quindimil et al. [29] studied the effect of the active metal composition in bimetallic $Ni-Ru/Al_2O_3$ catalysts with 12 wt% Ni and variable Ru loading, and concluded that 1 wt% Ru is a desirable loading amount, as it leads to an increase in the Ni dispersion, reducibility, and CH_4 yield. In another work by Pan et al. [30], the optimal Ni loading in Ni/CeO_2 catalysts was initially found to be 20 wt%. An approach was then followed to further increase the activity of this catalyst by introducing small Ru amounts. They found that just a very small Ru loading (0.2 wt%) was enough to achieve a maximum promotion in the low-temperature catalytic activity and reducibility. It can thus be envisaged, that a similar approach regarding the Ru:Ni bimetallic composition can also be applied for DFMs used in the ICCU-Methanation process.

This work is thus focused on the preparation of bimetallic Ru-Ni DFMs with low Ru loadings, supported on porous Na_2O/Al_2O_3, and their performance during ICCU-Methanation. To the best of our knowledge, it is the first one to systematically study the Ru:Ni bimetallic composition in bimetallic DFMs for the integrated CO_2 capture and conversion, while also providing a thorough material characterization (X-ray diffraction (XRD), N_2 physisorption, H_2 temperature programmed reduction (H_2-TPR), H_2 temperature programmed desorption (H_2-TPD), CO_2 temperature programmed desorption (CO_2-TPD), H_2 temperature programmed surface reaction (H_2-TPSR), transmission electron microscopy (TEM), high-angle annular dark-field scanning transmission electron microscopy (HAADF-STEM) with energy dispersive X-ray spectroscopy (EDS) mapping, X-ray photoelectron spectroscopy (XPS), and X-ray absorption spectroscopy (XAS)), coupled with in-situ diffuse reflectance infrared fourier-transform spectroscopy (in-situ DRIFTS) mechanistic experiments and computational fluid dynamics (CFD) modelling. By keeping the Ni loading at 20 wt% and introducing small Ru loadings (0.1–1 wt%), it is found that even a miniscule amount of Ru (i.e., 0.1–0.2 wt%) can drastically promote the active metal reducibility and the CH_4 production kinetics, as well as increase the overall CH_4 yield and the resistance to O_2 during CO_2 capture, with 0.2 wt% Ru providing the maximum promoting effect. A CFD model is also developed that can validate the experimental data and predict the effect of different parameters on the ICCU-Methanation performance.

2. Experimental

2.1. Material synthesis

A Pechini sol-gel method was used to prepare the support. $Al(NO_3)_3{\cdot}9H_2O$ was initially added in d-H_2O under continuous stirring. Citric acid and then ethylene glycol were added with the molar ratio of ethylene glycol, citric acid, and metal cations (Al^{3+}) being 3:1.5:1. Afterwards, the temperature of the solution was raised to 80 °C to promote the Al-citrate complex formation and the evaporation of water, leading finally to polycondensation between the hydroxyl and carboxyl groups and the formation of a viscous polymeric network. The viscous syrup was subsequently overnight dried at 120 °C and then calcined at 500 °C for 4 h, with an intermediate temperature hold step at 400 °C for 1 h. The adsorption-active (Na_2O) phase was then introduced to the support via wet impregnation. Initially, $NaNO_3$ in a calculated amount (for a 12 wt% "Na_2O" loading) was dissolved in d-H_2O under stirring. The support was then dispersed in the solution under stirring and the mixture was transferred to a rotary evaporator for water removal. Lastly, drying of the leftover solid at 120 °C overnight and calcination at 500 °C for 4 h yielded the Na_2O/Al_2O_3 adsorbent material (NaAl).

The Ni phase was then introduced via wet impregnation on the NaAl (Na_2O/Al_2O_3) adsorbent material, using $Ni(NO_3)_2{\cdot}6H_2O$ in a calculated amount to achieve the desired 20 wt% Ni loading. The dried powder after impregnation was calcined at 400 °C for 4 h. For the bimetallic Ru-Ni DFMs, Ru was incorporated via a subsequent wet impregnation step on the monometallic Ni-based DFM (20 wt% Ni) using a $Ru(NO)(NO_3)_x(OH)_y$ solution and with calcination performed at 250 °C for 4 h. A monometallic Ru reference material (0.2 wt% Ru) was also prepared without the prior Ni impregnation step. The calcined DFMs were finally reduced in-situ (under 10% H_2/Ar) for 1 h at 400 °C to obtain the reduced DFM counterparts.

2.2. Material characterization

XRD was performed on a Bruker Discover D8 apparatus (Bruker-AXS) using a Cu $K_{\alpha 1}$ radiation at 40 kV and 25 mA. In order to calculate the crystallite sizes of the various phases (NiO and metallic Ni^0), the Scherrer equation was applied following Voigt fitting of the respective crystalline reflections.

N_2 adsorption-desorption was performed using an Autosorb iQ instrument (Quantachrome instruments/Anton Paar) at 77 K (Physisorption mode). At first, outgassing was carried out for 4 h at 300 °C. The Brunauer-Emmett-Teller (BET) method was used to calculate the specific surface area values (p/p^0 = 0.07–0.3) and the non-local density functional theory (NLDFT) method was used to extract the pore size distribution graphs. The silica cylindrical pores model was applied on the adsorption branch (software ASiQ-Win) [32].

H_2-TPR was also carried out in the Autosorb iQ instrument (TCD mode). After pretreatment under He flow at 400 °C for 1 h and cooldown to room temperature, 10% H_2/N_2 (50 mL min^{-1}) was flown through the material and the temperature was gradually increased up 900 °C using a 10 °C min^{-1} temperature ramp, under continuous monitoring of the thermal conductivity detector (TCD) signal. Afterwards, experiments were also conducted after prior reduction (10% H_2/N_2) and then oxidation (20% O_2/Ar) pretreatments at 400 °C, to allow for the precursor decomposition and the formation of supported NiO-RuO_x oxides. A 1 h intermediate hold step at 400 °C was also introduced in this case. The TCD was calibrated following reduction of known amounts of CuO. Lastly, additional H_2-TPR experiments with 1 h temperature hold at 400 °C were also carried out for some materials in a packed bed reactor system (10% H_2/Ar flow), so that the gases exiting the reactor could be monitored via mass spectrometry (MS) using an on-line QMS 300 Prisma MS analyzer (Pfeiffer).

H_2-TPD was performed at the same instrument (Autosorb iQ). After material reduction at 400 °C with 10% H_2/N_2 for 1 h, He was flown for 30 min at 400 °C. The material was then cooled down to room temperature under He flow and then 10% H_2/N_2 was flown again through the material for 20 min for the H_2 adsorption. Afterwards, after purging with N_2, the temperature was gradually increased with a 10 °C min^{-1} ramp up to 900 °C under N_2 flow, under continuous monitoring of the TCD signal. TCD calibration was performed via pure H_2 pulses at a constant N_2 flow.

CO_2-TPD was also carried out at the same instrument. After reducing the materials at 400 °C with 10% H_2/N_2 for 1 h and flowing He for 5 min, 10% CO_2/Ar then flowed for 30 min at 400 °C (for the CO_2 adsorption to occur at an elevated temperature) and also during cooldown to room temperature. After He purge, the temperature was slowly increased to 900 °C with a ramp of 10 °C min^{-1} under He flow, under continuous monitoring of the TCD signal. TCD calibration was performed via pure CO_2 pulses at a constant He flow. Peak deconvolution for the calculation of the population of basic sites of different strength was performed via the QCfit option of the TPRWin software (Quantachrome instruments/Anton Paar).

H_2-TPSR was performed in a packed bed reactor system equipped with an on-line QMS 300 Prisma analyzer (Pfeiffer). After reducing the materials at 400 °C with 10% H_2/Ar for 1 h and then Ar purge for 5 min, 10% CO_2/Ar was flown for 30 min (for the CO_2 adsorption to occur at an elevated temperature) and also during cooldown to room temperature. Afterwards, following Ar purge, 10% H_2/Ar was flown again, and the temperature was slowly raised to 900 °C with a ramp of 10 °C min^{-1}, while the MS signal was continuously monitored. MS calibration was previously performed using certified gas mixtures diluted in Ar.

TEM was carried out using a T20 FEI-Tecnai microscope (200 kV) that had a LaB_6 electron source and "SuperTwin®" objective lens enabling point-to-point resolution of 0.24 nm. HAADF-STEM along with EDS analysis were carried out using an Analytic XFEG FEI Titan electron gun microscope (300 kV) that contained a Cs-probe (CEOS) with the ability of electron probe formation with 0.09 nm mean size.

XPS was carried out using a ThermoFisher K-alpha machine equipped with an X-ray gun generating monochromatic energy of 1500 eV. Sample preparation involved applying a stroke of the sample onto carbon tape and attaching it to the sample holder. The sample holder was then transitioned from the entry chamber to the analysis chamber onto a stage once the pressure dropped below 2×10^{-7} Pa. The analyzer selected electrons based on their kinetic energies, measuring counts within a fixed range of binding energies.

XAS was performed on the BM31 at the Swiss-Norwegian beamlines (SNBL)/ESRF in Grenoble (France). A continuous scan mode was employed using a Si(111) LN_2-cooled double crystal monochromator (DCM). The unfocussed beam size at the sample position was ca. 3 mm W × 300 μm H. Ni metal (*K*-edge at 8332.8 eV) foil and Ru metal (*K*-edge at 22117.2 eV) powders were used as standards for energy calibration and the measurements were performed in transmission geometry using optimized pre-filled ion chambers as detectors. The samples were manipulated under air atmosphere to make pellets from a mixture of ca. 30 mg catalyst powder and 70 mg cellulose as a filler and X-ray transparent material. They gave rise to perfect transmission samples at the Ni *K*-edge (edge step around 1); for the measurement, the samples were sandwich-taped between 50 μm sticky kapton films. On the other hand, the Ru *K*-edge measurements were carried out in both transmission (using ion chambers) and fluorescence geometry (Vortex SDD with XIA Falcon X fast digital multichannel analyzer electronics as detector system), and we opted to show the fluorescence data because of the better data quality generated by the low Ru loading, which rendered the material slightly too transparent at the Ru edge. No corrections were applied onto the fluorescence results, since the data were similar in terms of features intensity/position to the transmission measurements. Data reduction protocols, i.e., background removal, normalization and averaging (more scans were averaged for better S/N, especially at the Ru *K*-edge), truncation/deglitching, etc. were performed using the Athena software from the Demeter package [33].

In-situ DRIFTS was performed on a Nicolet 8700 spectrometer (Thermo Scientific) with a TRS-detector (LN-MCT), equipped with a DRIFT-cell (high-temperature) with CaF_2 windows (HVC praying mantis Harrick). The sample spectra were recorded via the accumulation of 128 scans (4 cm^{-1} resolution) under different gas flows, i.e., 10% CO_2/He for CO_2 adsorption, He for purge/flushing, and 10% H_2/N_2 for reduction/hydrogenation. In a typical experiment, the material was loaded in the reaction cell and initially reduced at 400 °C, followed by setting the temperature to the desired value (300 or 400 °C). Spectra collection was then carried out under the different gas flows.

2.3. Material testing

The experiments regarding the ICCU-Methanation process were performed in a packed bed reactor (quartz glass, I.D. = 0.9 cm), as described in Ref. [13]. In short, after reduction of 0.2 g of the DFM at 400 °C for 1 h with 10% H_2/Ar, the reactor temperature was set to the required value. For the CO_2 adsorption step, 50 mL min^{-1} of 10% CO_2/Ar flowed for 15 min. This was followed by 5 min of 50 mL min^{-1} Ar purge. For the hydrogenation step, 50 mL min^{-1} of 10% H_2/Ar flowed for 30 min. This was followed by another 5 min of Ar purge. Gas analysis of the reactor effluent was carried out with a QMS 300 Prisma analyzer (Pfeiffer).

For the stability experiments under multiple adsorption-methanation cycles, the adsorption and methanation step durations were reduced to 10 and 20 min, respectively. For the cycles performed under an oxidizing CO_2 capture atmosphere, the feed during the CO_2 adsorption step consisted of 10% CO_2, 10% O_2 balance Ar.

For the CO_2 adsorption step, the CO_2 adsorption capacity expressed in mmol g^{-1} was calculated as follows.

$$Q_{CO_2} = \frac{C_0 \cdot F_{in}}{W \cdot V_m} \int_0^t \left(1 - \frac{C_t}{C_0}\right) dt \quad (2)$$

where C_0 is the concentration of CO_2 in vol% at the inlet. F_{in} is the overall flow rate in mL min^{-1} at the inlet. C_t is the concentration of CO_2 in vol% at a specific time at the outlet. W is the DFM weight in g. V_m is the molar volume, which has a value of 22.414 mL $mmol^{-1}$.

For the hydrogenation step, the yields for CH_4, CO, and desorbed CO_2 expressed in mmol g^{-1} were calculated as follows.

$$Y_{CH_4} = \frac{F_{in}}{W \cdot V_m} \int_0^t \left(C_{CH_4,t}\right) dt \quad (3)$$

$$Y_{CO} = \frac{F_{in}}{W \cdot V_m} \int_0^t \left(C_{CO,t}\right) dt \quad (4)$$

$$Y_{CO_2} = \frac{F_{in}}{W \cdot V_m} \int_0^t \left(C_{CO_2,t}\right) dt \quad (5)$$

where $C_{CH_4,t}$, $C_{CO,t}$, and $C_{CO_2,t}$ are the flows of the CH_4, CO, and CO_2 gases in vol% at a specific time at the outlet.

Lastly, for the evaluation of the methanation reaction kinetics (calculation of the activation energy and reaction orders), continuous-flow CO_2 methanation experiments were carried out on the same reactor setup, but this time utilizing a gas chromatography analysis system for the gas analysis, as described in Ref. [4]. 0.06 g of the DFM diluted in quartz sand up to 1 g was added in the reactor, followed by reduction at 400 °C for 1 h under 10% H_2/Ar. The reaction gas mixture was initially composed of 10% CO_2, 40% H_2, and 50% Ar (volume), with a total flow of 100 mL min^{-1}. After the achievement of steady-state conversion at 230 °C, the reaction temperature was stepwise increased in 10 °C intervals. CO_2 conversion remained below 20% to ensure kinetically controlled reaction. For the calculation of the CO_2 and H_2 reaction orders, the CO_2 or H_2 concentration each time varied between 6%–14% and 30%–50%, respectively, while keeping the concentration of the other reactant and the total gas flow constant, at a fixed temperature corresponding close to 10% CO_2 conversion. The reaction metrics were calculated based on the formulae described in Ref. [34].

2.4. Process modelling

2.4.1. Reaction rates

CH_4 is generated through hydrogenation, according to the Sabatier reaction (Eq. (1)) [22]. The rate equation that describes the hydrogenation step and the formation of CH_4 during hydrogenation was developed according to the works of Bermejo-López et al. [25] and Falbo et al. [35].

$$r_{CH_4} = k_{CH_4}\left(P_{CO_2}^{n} P_{H_2}^{4n} - \frac{P_{CH_4}^{n} P_{H_2O}^{2n}}{\left[K_{eq}(T)\right]^{n}}\right) \quad (6)$$

where k_{CH_4} is the rate constant and $K_{eq}(T)$ is the equilibrium constant of the methanation reaction, respectively. The hydrogenation step was modelled by parametric fitting of the kinetic model, as proposed by Bermejo-López et al. [25].

2.4.2. Modelling methodology

Computational fluid dynamics (CFD) modelling was conducted in a packed bed reactor with the reaction kinetics installed through the chemistry interface and the mass and transport of reacting species modelled with the Transportation of Diluted Species interface along with the Reactive Pellet Bed feature, which takes into account convection, diffusion, and reaction in diluted solutions. The one-dimensional (1D) CFD model was developed with the temperature and concentration gradients occurring only in the axial direction and plug flow type being the transport mechanism that operates in this direction. The assumptions that were taken into account in the model design included: (a) isothermal and unsteady-state conditions, (b) very small/negligible pressure drop along the reactor length, (c) application of ideal gas law for gases, (d) constant axial fluid velocity inside the reactor with uniform transport coefficients and physical properties, and (e) material packing in powdered form inside the reaction zone. The reactor length was 30 cm. The internal diameter of the reactor was 0.9 cm, unless otherwise stated.

The mass balance equation given below incorporates the diffusion and convection for the species in the packed bed.

$$u_x \frac{\delta c_i}{\delta x} = D_{i,A} \frac{\delta^2 c_i}{\delta x^2} + D_{i,T} \frac{\delta^2 c_i}{\delta y^2} - J_i S_b \quad (7)$$

where D_i and J_i are the dispersion coefficient in the transverse or axial direction and the molar flux of the fluid in the powdered DFM, respectively.

S_b is the material active specific surface area that is in contact with the reactant fluids [36].

$$S_b = \frac{3}{r_{pe}}(1 - \varepsilon) \quad (8)$$

where ε is bed void fraction of material and r_{pe} is the size of material powder.

The assumption of film condition is made at the pellet-fluid interface. The mass flux associated with mass balance, which is considered as boundary condition, can be the rate determining step. The external mass transfer coefficient as described below is considered.

$$J_i = h_i(c_i - c_{i,ps}) \quad (9)$$

$$h_i = \frac{Sh \cdot D_i}{2r_{pe}} \quad (10)$$

$$Sc = \frac{\mu}{\rho \cdot D_i} \quad (11)$$

$$Re = \frac{2r_p \cdot \rho \cdot u_x}{\mu} \quad (12)$$

$$Sh = 2 + 0.552 Re^{1/2} Sc^{1/3} \quad (13)$$

where h_i and $c_{i,ps}$ are the external mass transfer coefficient and the species concentration on the surface of the material, respectively. For the reaction fluids, μ, ρ, and Sc are the density, viscosity, and

Schmidt number, respectively. *Re* is the Reynolds number. *Sh* is the Sherwood number [37,38].

The reaction takes place in the bed area that is packed with powder material. The mass balance regarding the powdered particle, as well as an additional predefined 1D dimension for the normalized radius ($r = r_{dim}/r_{pe}$), across the spherical shell, are expressed as following.

$$4\pi N\left\{r^2 r_{pe}^2 \varepsilon_{pe}\frac{\partial c_{pe,i}}{\partial t} + \nabla\left(-r^2 D_{i,eff}\nabla c_{pe,i}\right) = r^2 r_{pe}^2 R_{pe}\right\} \quad (14)$$

where N is number of particles. For the fluids inside the pores of the powder particle, $D_{i,eff}$ is the effective diffusion coefficient. $c_{pe,i}$ is the concentration for the different component species in the powder material, and R_{pe} is the reaction rate term.

In order to calculate the effective diffusivities for the different component species inside the powder material pores, Knudsen or bulk diffusion coefficients were taken into account [37].

$$D_{i,eff} = \frac{D_{i,AB}\cdot\Phi_p\cdot\sigma_c}{\tau} \quad (15)$$

where $D_{i,AB}$ is the diffusivity for the different fluid components in bulk. Φ_p is the powder material porosity. τ and σ_c are the tortuosity and constriction factor, respectively.

The boundary conditions for the packed bed reactor are displayed below.

$$\text{at } x = 0;\ c_i = c_{i,in} \quad (16)$$

$$\text{at } x = x_i;\ \frac{\delta c_i}{\delta x} = 0 \quad (17)$$

$$\text{at } r = 1;\ c_{i,p} = c_{i,ps} \quad (18)$$

$$\text{at } r = 0;\ \frac{\delta c_{i,p}}{\delta r} = 0 \quad (19)$$

The modelling software used in this work couples all the conservation equations, mass balances, and boundary conditions. The geometry of the packed bed reactor had a mesh that consisted of 50 domain elements and 2448 degrees of freedom. The solution provided was checked for higher degrees of freedom and no difference was obtained in the results, and thus the CFD results are mesh independent.

3. Results and discussion

3.1. Material characterization

3.1.1. Crystallinity and textural properties

XRD was first carried out for the reduced DFMs with low Ru loadings and 20 wt% Ni following the reduction pretreatment at 400 °C, and the results are included in Fig. 1a. The diffractograms display the reflections of crystalline γ-Al_2O_3 ($2\theta \approx 37.4°$, 46.0°, and 66.7°) from the support, NiO ($2\theta \approx 37.4°$, 43.4°, 63.1°, 75.5°, and 79.4°), and metallic Ni^0 ($2\theta \approx 44.5°$, 51.8°, and 76.4°). Reflections of any Na-containing crystalline phase due to the adsorption-active component are not observed, meaning that Na is most probably highly dispersed as Al-O^--Na^+ (or "Na_2O") sites over the γ-Al_2O_3 support [39–41]. Metallic Ru^0 is also not observed due to its low loading and high dispersion. Ni on the other hand exists as both oxidized NiO and as metallic Ni^0, meaning that part of it is reduced during the reductive pretreatment and part of it remains oxidized, especially for the monometallic Ni20 material [42,43]. Interestingly, the relative intensity of the Ni^0 metallic reflections to the NiO reflections is drastically increased as the Ru loading is increased. Significant differences can be observed even for the Ru0.1Ni20 sample, meaning that even 0.1 wt% of Ru addition can greatly increase the reduction degree of the NiO phase at 400 °C. Reflections attributed to $NiAlO_x$ (e.g., $NiAl_2O_4$) were not present, so that even if small $NiAlO_x$ nanocrystallites do exist, they are expected to be smaller than the XRD detection limit and/or their reflections overlap with those of other crystalline phases [44–46].

The crystallite sizes of NiO and metallic Ni^0 were calculated based on their reflections at $2\theta \approx 63°$ and 52°, respectively, following Voigt fitting, via the Scherrer equation (Table 1) [47], due to the overlap of the main NiO and Ni^0 reflections ($2\theta \approx 45°$ and 43°, respectively) with γ-Al_2O_3. The mean crystallite size of the metallic Ni^0 particles was found to be around 8–9 nm for all the reduced materials. Regarding NiO, the mean crystallite size is the largest for monometallic Ni20 at 13 nm, and is then reduced with increasing Ru loading in the materials down to 8 nm.

Fig. 1b shows the N_2 adsorption-desorption isotherms and the pore size distribution graphs of the reduced DFMs, while the BET surface area, average pore diameter, and pore volume values are shown in Table 1. All materials are mesoporous with type IV isotherms and a relatively high surface area (~95 $m^2\ g^{-1}$), which is required for heterogeneous catalytic reactions. All of them have a very similar porosity, probably since the very low Ru loading does not have the ability to significantly affect the material textural properties. The DFMs with 0.1–0.5 wt% Ru do however evidence a small increase in the surface area and pore volume compared to the monometallic Ni20 DFM.

3.1.2. Temperature-programmed reduction

H_2-TPR was then carried out by ramping up the temperature to 900 °C (Fig. 2a). The TPR profiles are characterized by an intense and large peak below 400 °C, ascribed to NiO reduction and the adsorbent phase activation, i.e., the removal of nitrates and other leftover precursor compounds, which influences the TCD signal [13,48–51]. For the monometallic Ni20 DFM, additional peaks can be observed at higher temperatures; the signal below 700 °C can be attributed to NiO reduction with a stronger metal-support interaction and the one above 700 °C to the reduction of Ni^{x+} species with a particularly strong metal-support interaction, namely those participating in $NiAlO_x$ (e.g., $NiAl_2O_4$) phase formation [21,45,49]. The presence of both crystalline NiO and metallic Ni^0 for Ni20 on the XRD following reduction at 400 °C (Fig. 1a) is in agreement with the H_2-TPR profiles, which show that only part of the NiO reduction occurs below 400 °C. Interestingly, upon the addition of very small Ru loadings, even 0.1 wt%, the main reduction peak, as well as the other NiO reduction events, shift toward lower temperatures. This means that the majority of oxidized NiO is now reduced below 400 °C, due to the promoted reducibility induced via the very small Ru loadings [20,52,53]. This is not the case however for the high-temperature reduction peak at >700 °C, which has a low but similar intensity in all samples, meaning that all of them are expected to display a rather similar amount of the $NiAlO_x$ phase, irrespective of the Ru loading. Lastly, the H_2-TPR profile of the bare NaAl (Na_2O/Al_2O_3) adsorbent is also shown to present a main TCD signal peak at approx. 540 °C, which, due to the lack of reducible NiO-RuO_x oxides, can be attributed solely to the reduction/decomposition of leftover precursor compounds (mainly nitrates due to the $NaNO_3$ precursor, but potentially also some carbonates), which now require a higher temperature to decompose compared to the DFMs [13,48].

In order to shed light into the precursor decomposition process and the evolution of various gases, H_2-TPR characterizations were also carried out for the Ni20 and Ru0.2Ni20 DFMs in the packed

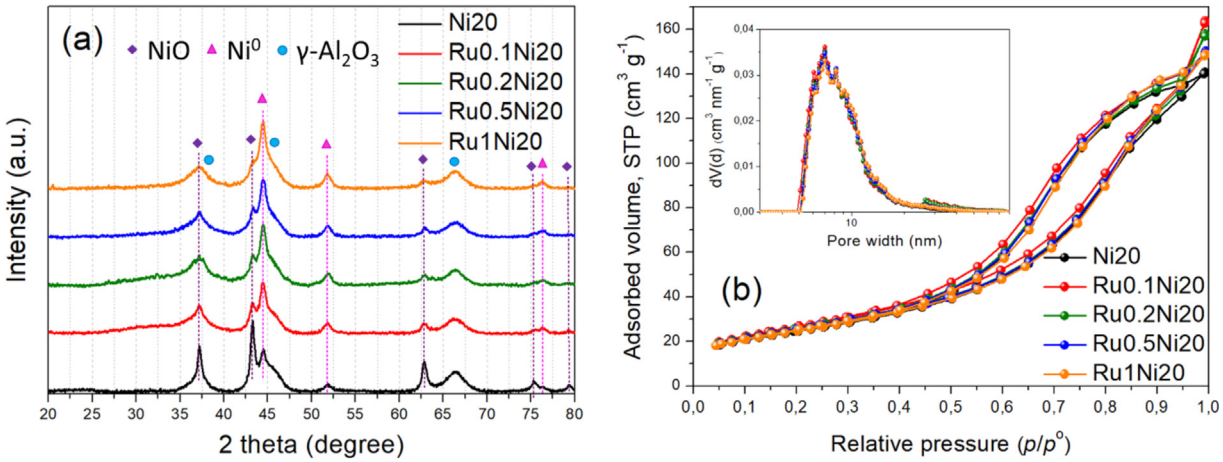

Fig. 1. (a) X-ray diffractograms and (b) N_2 adsorption-desorption isotherms with pore size distribution (inset) for the reduced DFMs.

Table 1
SSA (specific surface area), PV (pore volume), and APD (average pore diameter) obtained via N_2 physisorption for the reduced DFMs. Crystallite sizes (Φ) for NiO and metallic Ni^0 calculated via XRD (Scherrer). Mean nanoparticle size (d) determined via TEM analysis (nanoparticle size distribution histograms).

Material	SSA (m^2 g^{-1})	PV (cm^3 g^{-1})	APD (nm)	Φ_{NiO} (nm)	Φ_{Ni} (nm)	d (nm)
Ni20	89	0.22	9.8	13	8	12.3 ± 5.4
Ru0.1Ni20	96	0.25	10.5	11	9	8.1 ± 3.9
Ru0.2Ni20	92	0.25	10.6	9	9	9.7 ± 3.7
Ru0.5Ni20	91	0.23	10.1	9	9	9.6 ± 4.2
Ru1Ni20	89	0.23	10.3	8	9	7.8 ± 3.2

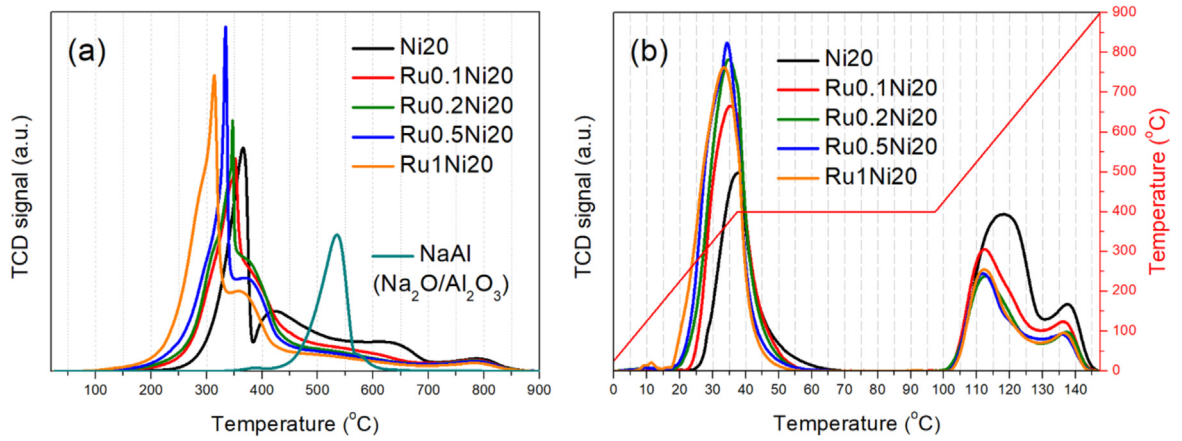

Fig. 2. H_2-TPR profiles of the DFMs and the NaAl adsorbent with (a) temperature rise up to 900 °C with prior pretreatment under inert gas and (b) temperature rise up to 900 °C with an intermediate temperature hold step at 400 °C for 1 h and with prior reduction and oxidation pretreatments.

bed reactor setup, where the outlet gases could be monitored via MS, using an 1 h hold step at 400 °C (Fig. S1). For the monometallic Ni20 DFM, an asymmetric rise in the signal for m/z = 17 when compared to the m/z = 18 signal at a temperature lower than 400 °C indicates a significant production of NH_3 following the hydrogenation of leftover nitrate precursors [13,15,21,49]. Then, the m/z = 28 signal is likely due to N_2 formation following NO_x reduction [13,54]. Small amounts of NO (m/z = 30) and likely N_2O (m/z = 44) are also produced, alongside a quite small CH_4 amount (m/z = 15), and at higher temperatures likely CO (m/z = 28), which could be ascribed to the reaction of some amount of pre-formed carbonates [13,15,49]. For the bimetallic Ru0.2Ni20 DFM, a significantly higher amount of NO (and also N_2O) is released during the nitrate precursor decomposition process, to the detriment of NH_3 formation. Furthermore, the reduction/precursor decomposition shifts toward lower temperatures. The nitrate precursors originate mainly from $NaNO_3$, but some quantity of leftover nitrates from the Ni and Ru precursor compounds could also remain in the samples following calcination. In all cases, it is quite clear that the reduction pretreatment at 400 °C is largely sufficient for the decomposition of the synthesis precursor compounds for the DFMs. The reason for the precursor decomposition in Ni20 and Ru0.2Ni20 DFMs occurring at lower temperatures compared to the bare NaAl adsorbent support (Na_2O/Al_2O_3, Fig. 2a) is the presence of the reducible metals (Ni and Ru), which can aid the reduction/decomposition of these precursor compounds (e.g., via the supply of reactive H-adatoms), as also evidenced by other works [13,45,48,49].

Afterwards, in order to exclude the contribution of the precursor decomposition and calculate the actual H_2 consumption values

that correspond to the active metal (NiO-RuO_x) reduction, H_2-TPR characterizations were performed following prior reduction and oxidation pretreatments at 400 °C (to decompose the precursor compounds) and also with a 1 h intermediate hold step at 400 °C (Fig. 2b). The H_2 consumption values up to the 400 °C isothermal step (Table 2) are indicative of the ability of the material to be reduced/activated at 400 °C following prior oxidation (e.g., under a flue gas atmosphere), and the promoting effect of the Ru presence, particularly up to 0.2 wt%, is demonstrated via the significant enhancement of the H_2 consumption values and the shift of the main reduction peak toward lower temperatures. The total H_2 consumption values up to 900 °C can be found in Table S1, and they roughly correspond to the theoretical values required for NiO-RuO_x reduction (e.g., 3.41 mmol g^{-1} theoretical value for monometallic Ni20). The active metal (NiO-RuO_x) reduction degree at 400 °C can then be calculated as the ratio between these two values (Table S1). It starts from as low as 42% for the monometallic Ni20 DFM and is then substantially increased up to 69% for Ru0.2Ni20 (0.2% Ru) and 70% for Ru1Ni20 (1% Ru). For the bimetallic DFMs, we could assume that RuO_x is totally reduced prior to 400 °C. When subtracting its contribution (as RuO_2 reduction), the NiO reduction degree at 400 °C still has the same values when rounded to the whole as the combined NiO-RuO_x reduction degree (much lower Ru loading compared to Ni). The great increase in the NiO reduction degree upon Ru addition, as well as the shift of the main reduction event, are suggested to occur via the initial reduction of the more reducible Ru (RuO_x), which can then accelerate/enhance the reduction of Ni-species, enabling it to proceed at lower temperatures than it would typically proceed for monometallic Ni materials in the absence of Ru. This is proposed to occur by improving the H_2 supply/H_2 dissociation and spillover to nearby Ni species, as also suggested by other works [20,21,29,52].

3.1.3. Temperature-programmed desorption of H_2 and CO_2

H_2-TPD was then performed in order to understand the material interaction with H_2 and estimate the population of metallic surface sites that are available following reduction at 400 °C (Fig. 3a) [34]. The H_2-TPD profiles present two peaks, one at lower temperatures (<350/400 °C) and one at higher temperatures (>350/400 °C). According to the literature [21,29,55], the low-temperature peak can be attributed to the desorption of H_2 that was previously adsorbed on metallic surface sites, whereas the high-temperature peak can be assigned to the desorption of spillover H_2, or H_2 present on the subsurface layers of the support. Therefore, the amount of desorbed H_2 from the low-temperature peak (<400 °C) can be used to estimate the availability of surface metallic sites and the metallic surface area [21,29,55].

It is apparent, that the desorbed H_2 amount below 400 °C (Table 2) increases greatly upon the introduction of just 0.1 wt% Ru (Ru0.1Ni20), and then further increases for 0.2 wt% Ru (Ru0.2Ni20) and for higher Ru loadings. The active metallic surface area (including Ni and Ru surface atoms) was then calculated based on the amount of desorbed H_2 below 400 °C (Table S1) [56], and is found to greatly increase from approx. 4.4 m^2 g^{-1} for the monometallic Ni20 DFM up to 8.7 m^2 g^{-1} for Ru0.2Ni20 and 9.7 m^2 g^{-1} for Ru1Ni20. Additionally, the desorbed H_2 amount below 400 °C and the active metal (NiO-RuO_x) reduction degree at 400 °C were used to obtain the active metal (Ni and Ru) dispersion values (Table S1) [52,56,57]. For the monometallic Ni20 DFM, the active metal (Ni) dispersion was found to be the lowest, at 16%, which would yield a mean metallic Ni^0 particle size of approx. 9 nm [56,57] (in good agreement with the value obtained from XRD). For the bimetallic DFMs, the active metal dispersion (for both Ni and Ru) is calculated to be higher, at roughly 19%–20%. Besides a potential improvement in the Ni dispersion, these values are expected to be brought up by the significantly higher dispersion of the Ru metal component (compared to Ni), assuming that Ru is not exclusively alloyed with Ni [29,52]. As previously mentioned, the improvement of the H_2 dissociation and spillover in the materials upon Ru addition can in turn promote the reduction of adjacent Ni-species and enable the overall NiO reduction to take place at lower temperatures [20,21,29,52].

CO_2-TPD was also used to estimate the population and strength of the surface basic sites that are available for CO_2 chemisorption (Fig. 3b, Table 2) [58]. In our case, the desorbed CO_2 amount at various temperatures can be divided into CO_2 desorbed from weak basic sites (T < 300 °C), moderately-strong basic sites (300 °C < T < 650 °C), and strong basic sites (>650 °C) (Table S2). The weak basic sites correspond to weakly-bound carbonates and bicarbonates, the moderately-strong basic sites correspond to the majority of adsorbed CO_2 over the adsorption-active Al-O^--Na^+ sites as carbonates (mostly bidentate), and the strong basic sites correspond to rather strongly-bound bulkier Na_2CO_3-type carbonates [13,41,49]. All materials contain mostly basic sites of moderate strength (calculated following peak deconvolution in TPRWin, Table S2). The calculated total surface basicity is relatively high, at approx. 1.2 mmol CO_2 per gram of material (Table 2). It can also be observed that the CO_2-TPD profiles of the different materials are quite similar, with only minor differences. As a result, the material surface basicity and thus, the CO_2 adsorption capacity, are mainly influenced by the presence of surface Al-O^--Na^+ sites due to the adsorbent component ("Na_2O"), and are only slightly affected by the availability of additional surface metallic sites [13,40,48], considering that sufficient adsorbent activation via precursor decomposition is achieved following the reduction pretreatment at 400 °C, as shown during H_2-TPR (Fig. S1).

3.1.4. Temperature-programmed surface reaction

H_2-TPSR was then utilized in order to study the CH_4 formation ability of the DFMs from pre-adsorbed CO_2 as a function of temperature (Fig. 4). The peak CH_4 formation temperature of the monometallic Ni20 DFM is found to dramatically reduce even after just 0.1 wt% Ru addition, from approx. 300 °C for Ni20 to 260 °C for Ru0.1Ni20 (around 40 °C drop). For 0.2 wt% Ru (Ru0.2Ni20), the peak CH_4 concentration is significantly increased, while for higher Ru loadings, the peak CH_4 concentration slightly drops. In general, a lower temperature for CH_4 formation during H_2-TPSR means that

Table 2
H_2 consumed during H_2-TPR with prior reduction/oxidation pretreatments and 1 h hold step up to 400 °C, H_2 desorbed during H_2-TPD up to 400 °C, total CO_2 desorbed during CO_2-TPD, and total CH_4 produced during H_2-TPSR.

Material	H_2 consumed (up to 400 °C, mmol g^{-1})	H_2 desorbed (up to 400 °C, mmol g^{-1})	CO_2 desorbed (mmol g^{-1})	CH_4 produced (mmol g^{-1})
Ni20	1.46	0.057	1.17	0.83
Ru0.1Ni20	2.05	0.099	1.22	0.85
Ru0.2Ni20	2.40	0.111	1.25	0.86
Ru0.5Ni20	2.47	0.115	1.22	0.82
Ru1Ni20	2.53	0.125	1.21	0.80

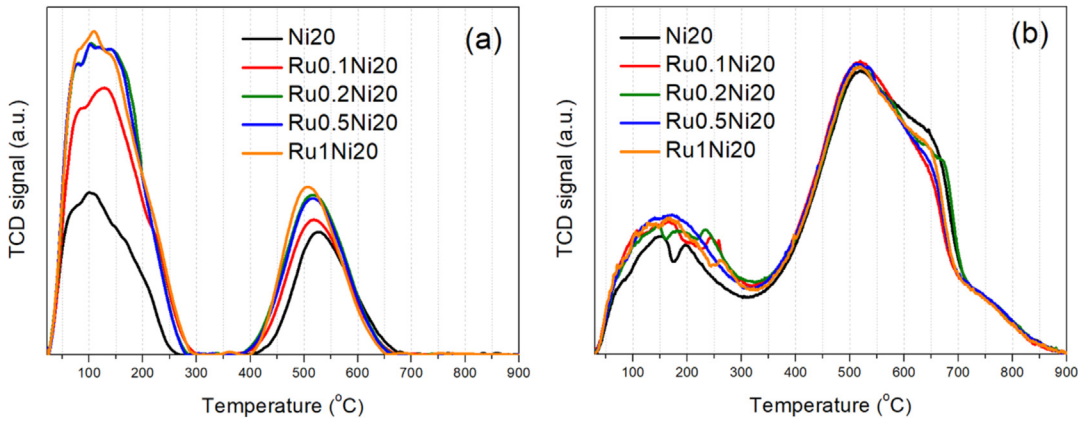

Fig. 3. (a) H_2-TPD and (b) CO_2-TPD profiles of the reduced DFMs.

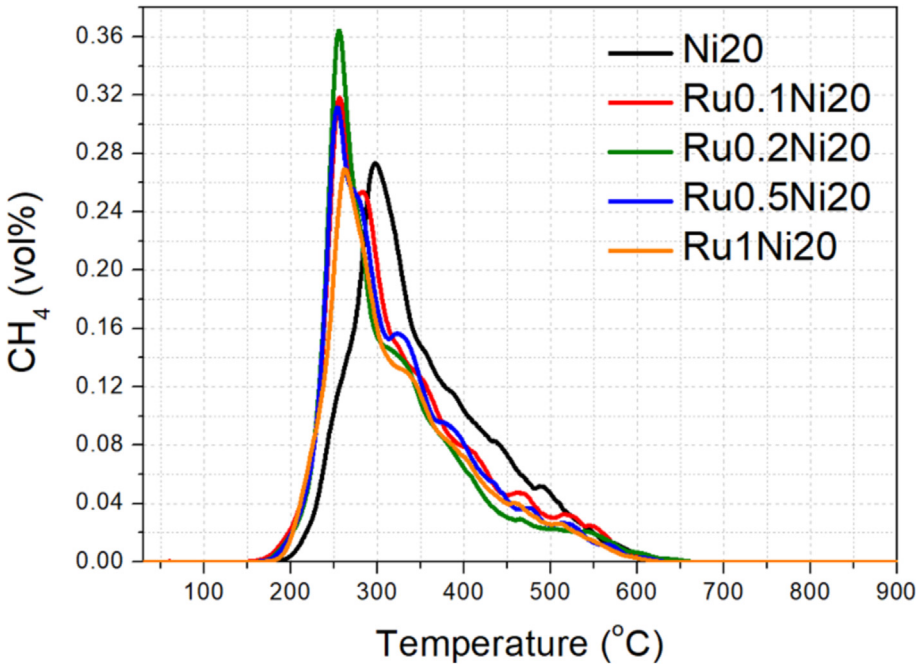

Fig. 4. CH_4 formation during the H_2-TPSR experiments for the reduced DFMs.

the material will be more active at lower temperatures during the ICCU-Methanation isothermal operation [13,21]. The total CH_4 production is the highest for Ru0.2Ni20 (0.86 mmol g^{-1}), though the differences in the total CH_4 yield between the materials are minor (Table 2).

The CO formation and the desorption of unreacted CO_2 are shown in Fig. S2 and Table S3. CO formation from pre-adsorbed CO_2 is very low at the low-temperature regime, due to the high CH_4 selectivity of the DFMs at these temperatures. CO production then increases at higher temperatures (>550 °C) due to the endothermic reverse water-gas shift reaction [59,60], but still, the total amount of produced CO is minor. The amount of unreacted desorbed CO_2 on the other hand is high at the low-temperature regime (<250 °C), due to the desorption of CO_2 from the weak basic sites without it being hydrogenated and converted to other products.

3.1.5. Electron microscopy characterization

TEM analysis was carried out for the reduced DFMs (Fig. 5). It can be observed that the support has a quite porous nanostructure, allowing for the dispersion of small and medium-sized nanoparticles. These nanoparticles can be easily located due to the high *Z*-contrast and are primarily metallic Ni ones, along with some oxidized NiO particles that can hardly be distinguished from the reduced/metallic ones via TEM. Ru could also potentially form small particles, alloy with Ni, or be finely dispersed over the support. All materials have a similar morphology, and the supported nanoparticles have a high size polydispersity, ranging from a few nanometers up to approx. 20 nm in diameter. The corresponding histograms for the nanoparticle size distribution are shown in Fig. S3 and the mean nanoparticle size values are listed in Table 1. The monometallic Ni20 DFM presents a larger mean nanoparticle size (approx. 12 nm) compared to the bimetallic DFMs, but this value could also be influenced by the oxidized (NiO) particles, which, according to the XRD results, can be larger than the metallic Ni^0 particles in this sample. For the bimetallic Ru-Ni DFMs, the mean nanoparticle size is similar, at approx. 8–10 nm, in good agreement with the results obtained from XRD.

HAADF-STEM analysis and EDS elemental mapping were also performed. The low-magnification EDS elemental mapping images

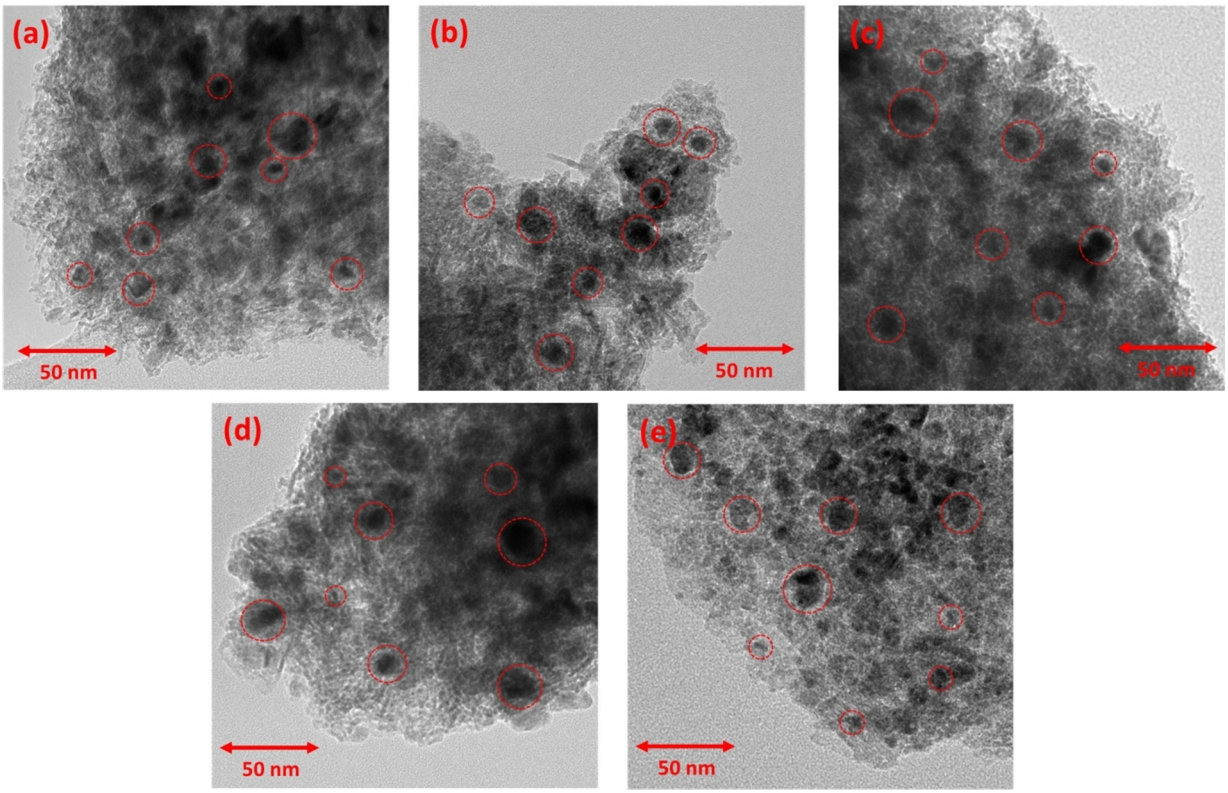

Fig. 5. TEM images of the reduced DFMs: (a) Ni20, (b) Ru0.1Ni20, (c) Ru0.2Ni0, (d) Ru0.5Ni20, and (e) Ru1Ni20. The location of some metallic nanoparticles is indicated by red circles.

for the Al, O, Na, and Ni elements in the monometallic Ni20 and the bimetallic Ru0.2Ni20 and Ru1Ni20 DFMs (with 0.2 wt% Ru and 1 wt% Ru, respectively) can be found in Fig. S4. The existence of small and medium-sized Ni-rich nanoparticles, along with some larger ones in certain regions, can be verified via the Ni elemental mapping images in these samples, while a considerable amount of Ni is also dispersed over the support [61,62], making the localization of the Ni^0-AlO_x (Ni nanoparticle-support) interface rather difficult. Furthermore, the homogeneous dispersion of Na throughout the samples (absence of large segregated Na_2O domains) proves the existence of an abundance of adsorption-active sites, namely CO_2-philic Al-O^--Na^+ or highly dispersed "Na_2O" [13,39–41].

Regarding the dispersion of Ru in Ru0.2Ni20 (0.2 wt% Ru) and Ru1Ni20 (1 wt% Ru), it is hard to be evaluated due to its low loading. Therefore, additional higher magnification images were acquired (Fig. 6), showing the Ni and Ru EDS elemental mapping for the reduced Ni20, Ru0.2Ni20, and Ru1Ni20 DFMs. The existence of small and medium-sized Ni nanoparticles is again observed in all cases, while Ru is generally found to be highly dispersed over the bimetallic materials and does not exclusively form Ru-Ni alloys [52], although certain regions do reveal the formation of rather small, segregated Ru particles (Fig. 6d and f). It can be stated that Ru forms single atoms/small clusters that are highly dispersed both over the Na_2O/Al_2O_3 support [52,61,63], as well as over the small and medium-sized Ni particles (e.g., as single atom alloys) [52,64,65], while a preferential concentration of Ru atoms at the Ni^0-AlO_x interface cannot be verified, due to the complexity of the sample system/composition. As previously mentioned, besides the highly dispersed state of Ru, some sample regions also reveal the segregation of Ru in the form of Ru particles. This segregation is much more pronounced in the Ru1Ni20 sample with the highest Ru loading (1 wt%), compared to the Ru0.2Ni20 sample with a much lower Ru loading (0.2 wt%), and can in turn lead to a reduction in the surface-available Ru sites, or the Ru-Ni bimetallic interaction/synergy for Ru1Ni20.

3.1.6. X-ray photoelectron spectroscopy

XPS was then performed for the reduced Ni20, Ru0.2Ni20, and Ru1Ni20 DFMs with 0 wt%, 0.2 wt%, and 1 wt% Ru loadings, respectively. The Ni 2*p* and Ru 3*p* spectra are shown in Fig. 7, whereas the O 1*s*, Al 2*p*, and Na 1*s* spectra can be found at the Supplementary Material (Fig. S5). The Ni 2*p* spectra (Fig. 7a) reveal the presence of different Ni species, i.e., metallic Ni^0 starting from a lower binding energy (BE), then the oxide phase of NiO, and then, at even higher BE, the peak can be ascribed to the contribution of $NiAlO_x$ species (e.g., $NiAl_2O_4$), but also to $Ni(OH)_2$ and even Ni^{3+} species due to Ni surface oxidation and hydroxylation following air exposure (ex-situ XPS characterization) [52,66,67]. The lower intensity (to some extent) of this high BE peak for the Ru0.2Ni20 and Ru1Ni20 samples, compared to Ni20, can infer a slightly lower contribution of $NiAlO_x$ species upon Ru presence, for the DFMs after the material reduction. Looking at the Ru 3*p* XPS spectra (Fig. 7b), there are no evident peaks for the Ru0.2Ni20 DFM, due to the very low concentration of Ru. For the Ru1Ni20 DFM however, there is an evidently high contribution of metallic Ru^0 (e.g., present in Ru particles), with the contribution of oxidized Ru^{x+} likely originating chiefly from the air exposure prior to the ex-situ XPS characterization [68,69].

Regarding the O 1*s* spectra (Fig. S5a), there are different oxygen species that exist in the materials, namely lattice oxygen in the Al_2O_3 lattice [66,67], adsorbed oxygen species in the form of surface hydroxyls/carbonates, and even physiosorbed H_2O following air exposure [34,52,67]. The Al 2*p* spectra (Fig. S5b) can be ascribed to Al^{3+} ions in the Al_2O_3 lattice and a small contribution of AlO(OH)/$Al(OH)_x$ species following air exposure and surface oxidation/hydroxylation [70], with the monometallic Ni20 sample

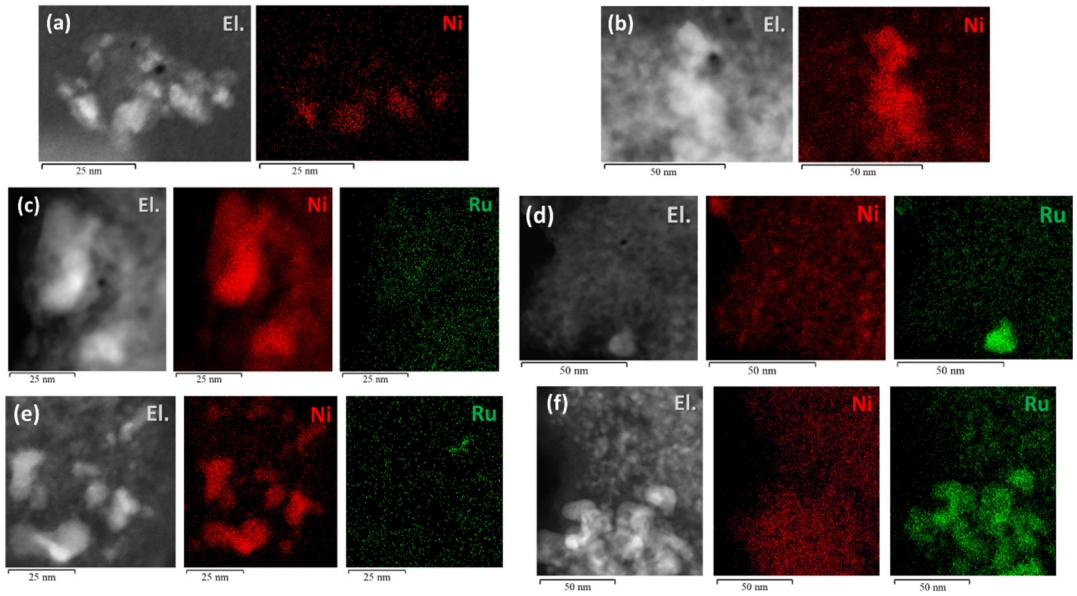

Fig. 6. HAADF-STEM electron images along with EDS elemental mapping images regarding the Ni and Ru elements for the reduced (a, b) Ni20, (c, d) Ru0.2Ni20, and (e, f) Ru1Ni20 DFMs.

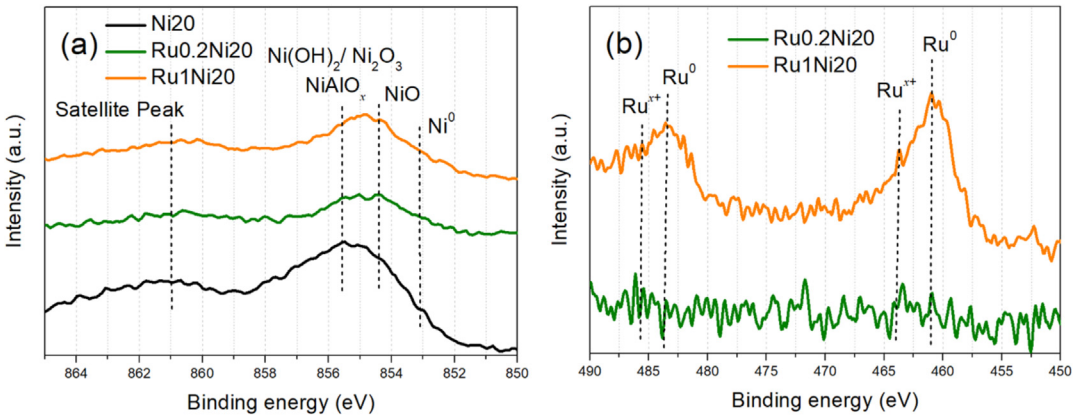

Fig. 7. (a) Ni 2*p* and (b) Ru 3*p* XPS core level spectra of the reduced Ni20, Ru0.2Ni20, and Ru1Ni20 DFMs.

appearing more prone to this effect. Finally, the asymmetric form of the Na 1*s* peak (Fig. S5c) suggests the presence of different Na-species, namely Na^+ ions that are highly dispersed over the Al_2O_3 support oxide as Na-O-Al interfacial sites, and segregated Na^+ ions as Na_2O oxides, or NaOH formed following hydroxylation under air exposure [71,72]. The contribution of surface-segregated Na_2O/NaOH appears to be higher for the monometallic Ni20 DFM and lower for the bimetallic Ru0.2Ni20 and Ru1Ni20 DFMs, since the presence of Ru may affect the Na dispersion following the material reduction.

3.1.7. X-ray absorption spectroscopy

Lastly, XAS was carried out for the reduced monometallic Ni20 DFM, as well as for the reduced bimetallic Ru0.2Ni20 and Ru1Ni20 DFMs, with 0.2 wt% Ru and 1 wt% Ru, respectively (Fig. 8). It should also be noted that the Ni *K*-edge was measured in transmission mode and the Ru *K*-edge in fluorescence mode (due to the low Ru content). The Ni references were metallic Ni foil and NiO, while the Ru references were metallic Ru powder and RuO_2. The results at the Ni *K*-edge (Fig. 8a and b) indicate the contribution of both metallic Ni and oxidized Ni (NiO) in the reduced samples, due to the partial reduction of Ni [64,73]. The contribution of metallic Ni^0 is significantly increased upon Ru addition, as also described during the XRD and H_2-TPR results. It is hereby shown however, that the contribution of metallic Ni (Ni–Ni bonding), in comparison to that of oxidized Ni (Ni–O bonding), increases up to 0.2 wt% Ru addition (Ru0.2Ni20) without a further increase beyond that point for 1 wt% Ru (Ru1Ni20), meaning that the reducibility enhancement effect of Ru is maximized for just 0.2 wt% Ru addition. More specifically, the ratio between metallic Ni^0 and oxidized NiO (Ni^0:NiO, X-ray absorption near edge structure (XANES)) was determined to be 26%:74% for monometallic Ni20, 40%:60% for bimetallic Ru0.2Ni20, and 37%:63% for bimetallic Ru1Ni20. Additionally, an extended X-ray absorption fine structure (EXAFS) fit (not shown) of the Ni *K*-edge for the three materials using the Ni and NiO references was performed, and the values for the bond lengths and coordination numbers are displayed in Table S4.

The results at the Ru *K*-edge (Fig. 8c and d) show that the bimetallic Ru1Ni20 sample (with the highest 1 wt% Ru loading) displays a behavior that is quite similar to that of the metallic Ru^0 powder reference, albeit with a slight oxidized Ru character. The fourier-transform EXAFS (FT-EXAFS) spectrum also shows a

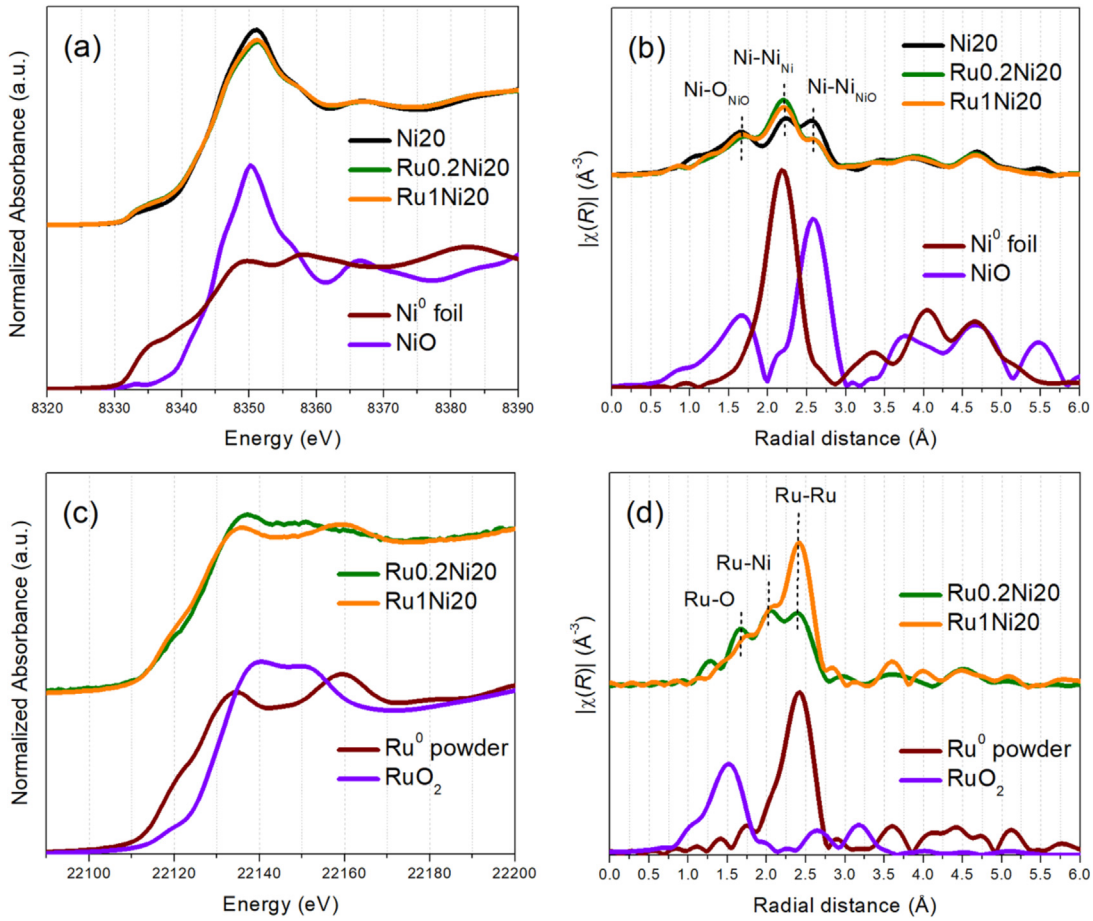

Fig. 8. (a) Ni *K*-edge XANES spectra, and (b) FT-EXAFS (not corrected for phase shift), (c) Ru *K*-edge XANES spectra, and (d) FT-EXAFS (not corrected for phase shift) of the reduced Ni20, Ru0.2Ni20, and Ru1Ni20 DFMs, along with those of reference samples.

quite high contribution of Ru–Ru bonding [31,65,70]. It can be assumed that this Ru–Ru contribution mainly comes from the Ru atoms present in (largely monometallic) Ru nanoparticles (in agreement with the electron microscopy results), or Ru–Ni bi-clusters, showing in fact a quite high percentage of Ru for Ru1Ni20 residing in aggregated form as small nanoparticles/clusters, and thus, not atomically dispersed. The interaction between Ru and Ni in the form of Ru-Ni alloy sites is also apparently quite small in comparison to the Ru–Ru contribution. However, for the sample with a significantly lower Ru loading (Ru0.2Ni20, 0.2 wt% Ru), there are additional prominent peaks in the FT-EXAFS spectrum besides that for Ru–Ru, and it also exhibits a higher oxidized Ru character. The largest FT-EXAFS peak for this sample, at lower radial distance than Ru–Ru, can be assigned to Ru–Ni bonding from Ru-Ni alloy (e.g., single atom alloy) sites (shorter bond length for Ru–Ni compared to Ru–Ru, depending also on the alloy composition) [31,64,65]. Moreover, an additional large peak at an even lower radial distance is ascribed to Ru–O bonding (oxidized Ru^{x+}), which can be formed from single Ru atoms at the Na_2O/Al_2O_3 support [63,74], or even from former metallic Ru atoms following ex-situ oxidation to some extent [64]. As such, Ru is better dispersed and exists in a variety of different states for Ru0.2Ni20, whereas it is largely found as Ru particles/clusters for Ru1Ni20. Fig. S6 shows the wavelet-transform EXAFS (WT-EXAFS) spectra of the Ru0.2Ni20 and Ru1Ni20 DFMs along with those of the Ru^0 powder and RuO_2 references, where it can be observed that the spectrum of the Ru1Ni20 DFM better matches that of the metallic Ru^0 powder reference, whereas Ru0.2Ni20 displays considerably more oxidized character.

3.2. Material testing

3.2.1. Effect of the Ru-Ni bimetallic composition

The materials with a different active metal composition (20 wt% Ni, and either 0, 0.1, 0.2, 0.5, or 1 wt% Ru) were initially evaluated at 300 °C (isothermal operation), since this is a temperature typically selected during the process of ICCU-Methanation in the literature [11–13,75,76]. Fig. 9a shows the values for the CH_4, CO, and CO_2 yield, and the CO_2 adsorption capacity for the DFMs at 300 °C. The CH_4 signal evolution with time is shown in Fig. 9b, while the cumulative CH_4 yield evolution with time during hydrogenation is displayed in Fig. 9c.

Interestingly, the CH_4 yield at 300 °C (Fig. 9a) increases greatly after the incorporation of very low Ru loadings (0.1 and 0.2 wt%), from 0.45 mmol g^{-1} for the monometallic Ni20 DFM, up to a maximum of 0.53 mmol g^{-1} for the bimetallic Ru0.2Ni20 DFM with just 0.2 wt% Ru. The total CH_4 yield then drops for higher Ru loadings down to 0.46 mmol g^{-1} for 1 wt% Ru, meaning that just 0.2 wt% Ru is sufficient to achieve the maximum promotional effect on the total CH_4 yield. Regarding the CO yield, it drops as the Ru loading increases, thereby promoting the CH_4 selectivity over CO. The initial CO_2 adsorption capacity and the amount of desorbed unreacted CO_2 during hydrogenation are similar between the DFMs.

The most profound change upon Ru incorporation in the material performance however, is evident in the so-called methanation kinetics. Upon the addition of very low Ru loadings, the peak CH_4 concentration during the hydrogenation step increases by 85% for 0.1 wt% Ru and 130% for 0.2 wt% Ru (compared to monometallic Ni20), as the CH_4 concentration signal becomes much sharper for

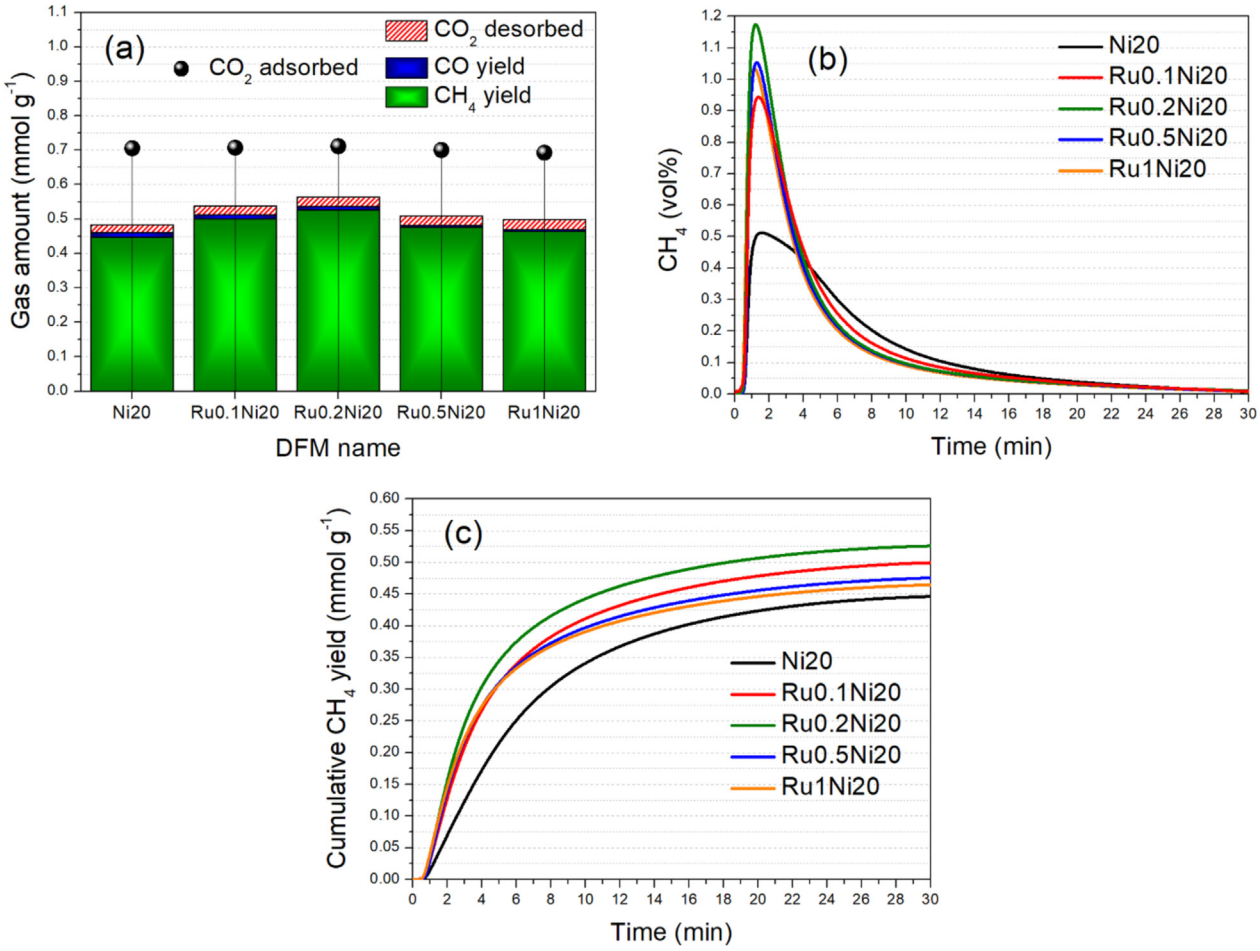

Fig. 9. (a) CH_4 yield, CO yield, CO_2 yield, and CO_2 adsorption capacity for the DFMs at 300 °C. (b) CH_4 signal evolution and (c) cumulative CH_4 yield evolution with time during hydrogenation.

the bimetallic Ru-Ni DFMs (Fig. 9b). Therefore, the addition of just a miniscule Ru amount in Ni-based DFMs can dramatically promote the methanation reaction kinetics of pre-adsorbed CO_2. The cumulative CH_4 yield also demonstrates this effect (Fig. 9c). For the example of Ru0.2Ni20 (0.2 wt% Ru), 85% of the overall CH_4 yield is reached after 10 min of hydrogenation, compared to just 75% for the monometallic Ni20 DFM.

An overview of the reactor outlet gas composition during a complete adsorption-methanation (adsorption-hydrogenation) cycle for the monometallic Ni20 DFM and the best-performing bimetallic Ru0.2Ni20 DFM at 300 °C can be found in Fig. S7. It is evident that CH_4 dominates the product concentration profile, as the CH_4 yield is much larger compared to the yield of CO and unreacted CO_2. CH_4 on the other hand is produced for a much longer duration, whereas the production of CO and the desorption of CO_2 take place right at the beginning of the hydrogenation process.

3.2.2. Effect of the operating temperature

The operating temperature effect during the process of ICCU-Methanation was then studied for the monometallic Ni20 DFM (20 wt% Ni) and the bimetallic Ru0.2Ni20 DFM (0.2 wt% Ru and 20 wt% Ni), which, at 300 °C, provided the highest CH_4 yield and the fastest methanation reaction kinetics (Fig. 10). Initially, we can observe that the CO_2 adsorption capacity decreases with increasing temperature, which can be ascribed to the exothermic character of CO_2 adsorption on the alkaline sites of the materials (i.e., Al-O^--Na^+ or "Na_2O" sites) [13,39,41,77]. The CH_4 yield on the other hand reaches a maximum value at 350 °C for Ni20 and at 300 °C for Ru0.2Ni20. The lower CH_4 production at 250 °C is attributed to the reduction in kinetic energy, which is required to drive forward the sluggish methanation process [78,79]. For the highest operating temperature (400 °C), the total CH_4 yield is also lower due to a smaller amount of pre-adsorbed CO_2 available for methanation in the first place, and the exothermic character of the CO_2 methanation reaction [41,78]. The CO yield remains low at the whole temperature range tested. When looking at the CH_4 concentration profiles and the cumulative CH_4 yield (Fig. 10c–f), it is also evident that CH_4 production at a lower temperature (250 °C) takes place quite slowly, and that the CH_4 signal reaches its peak long after the hydrogenation step has been initiated. The CH_4 concentration signal then becomes sharper up to a specific temperature (350 °C for Ni20 and 300 °C for Ru0.2Ni20), after which a further increase in temperature does not provide any additional benefits to the methanation reaction kinetics.

When comparing the two different materials (monometallic Ni20 and bimetallic Ru0.2Ni20), it is evident that the greatest difference between them lies in the low-temperature regime. In particular, the total CH_4 yield for Ru0.2Ni20 is 18% higher at 300 °C and 110% higher at 250 °C compared to Ni20, while at higher temperatures (350 and 400 °C), the total CH_4 yield is similar. The CH_4 production kinetics also demonstrates substantial differences between the two materials. At 250 °C for example, the CH_4 signal for Ni20 is quite flat and the CH_4 yield increases very slowly, while for Ru0.2Ni20 a clear peak can be observed at 250 °C, with the total

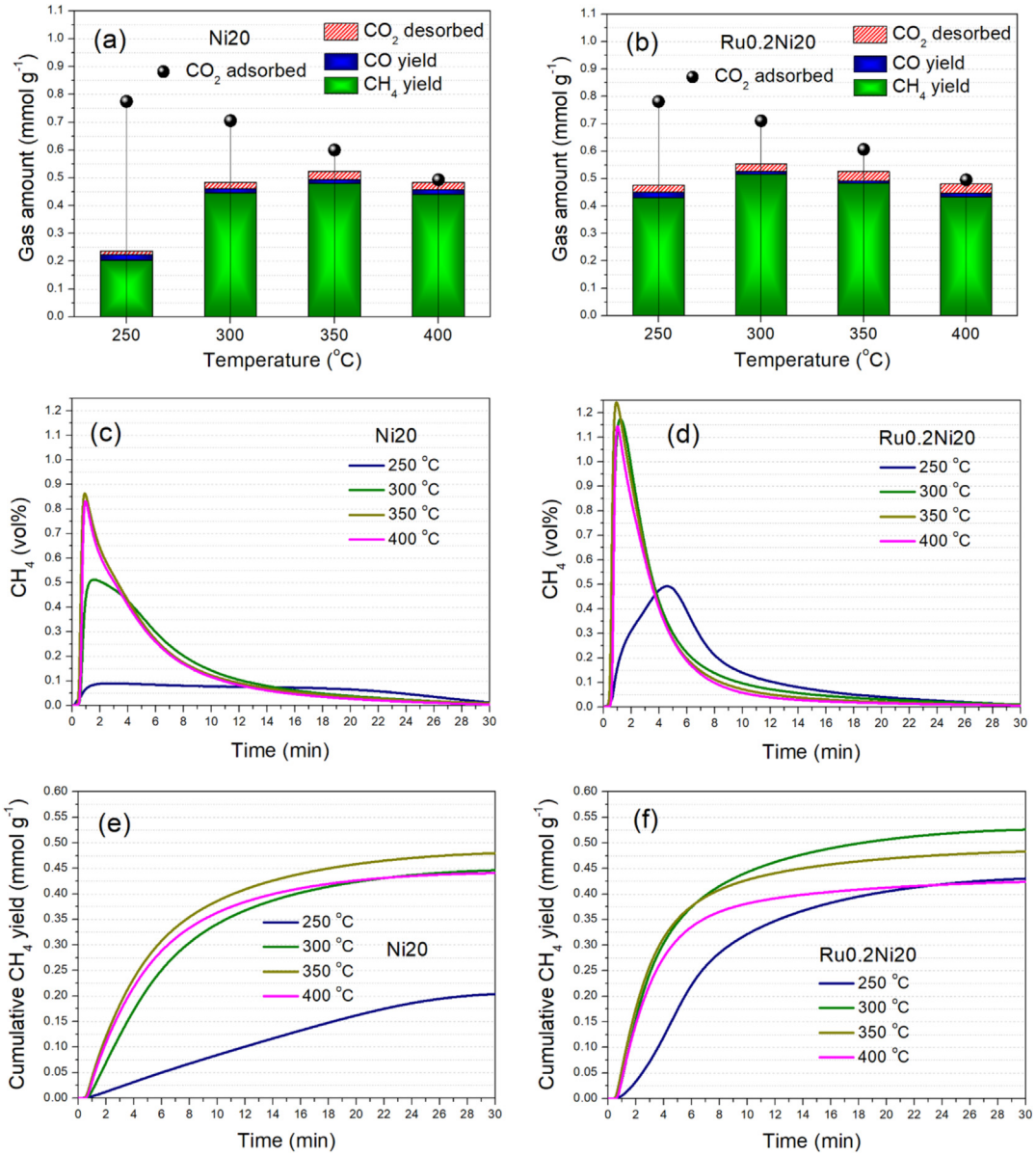

Fig. 10. (a, b) CH_4 yield, CO yield, CO_2 yield, and CO_2 adsorption capacity for the Ni20 and Ru0.2Ni20 DFMs at different operating temperatures. (c, d) CH_4 signal evolution and (e, f) cumulative CH_4 yield evolution with time during hydrogenation.

CH_4 yield being significantly higher, thereby corroborating the ability of Ru to promote the low-temperature methanation catalytic activity [28,30,52]. A similar, though less pronounced, trend is also observed at 300 °C. Even at the high-temperature regime (350 and 400 °C), the CH_4 concentration profile is quite sharper for Ru0.2Ni20 compared to Ni20, despite the final (total) CH_4 yield being rather similar.

It can be observed, that the differences between the DFMs become smaller as the reaction temperature increases. Therefore, additional experiments were also performed for the other bimetallic DFMs at the maximum operating temperature of 400 °C (Fig. S8). It is shown, that the total CH_4 yield is almost equivalent for all materials, and actually a very small decline upon Ru addition is observed. Similarly to the tests performed at 300 °C, the CO yield drops with increasing Ru loading, leading to a higher CH_4 selectivity over CO. Again, the main difference lies in the CH_4 production kinetics. Despite the CH_4 yield being similar for all materials, the CH_4 formation rate becomes considerably faster even after just 0.1 wt% Ru addition. For the example of Ru0.2Ni20, the peak CH_4 concentration is increased by 38% compared to Ni20, and the CH_4 concentration signal is much sharper.

Thereafter, in order to account for the methanation activity of Ru in the absence of Ni, a monometallic $Ru/Na_2O/Al_2O_3$ reference material without Ni (Ru0.2), with 0.2 wt% Ru (since 0.2 wt% Ru led to the highest performance in the bimetallic Ru-Ni DFMs), was prepared and evaluated for the ICCU-Methanation process in the 250–400 °C temperature range (Fig. S9). A significantly lower/miniscule CH_4 formation is observed at the low temperature range of 250–300 °C, which is increased at 350–400 °C, but still remains at quite low levels compared to the monometallic Ni20 and the bimetallic Ru-Ni DFMs (<0.35 mmol g^{-1}). This can be attributed to the overall much lower content for the catalytically active metal sites in the absence of the Ni phase [52]. It should also be noted, that the CO yield is significantly higher for Ru0.2 (CH_4 selectivity over CO <80%). Lastly, the kinetics of CH_4 formation during hydrogenation is negatively affected in the absence of Ni, since

CH_4 is formed at a quite slower rate over the Ni-free Ru0.2 reference material, with a much lower peak CH_4 concentration.

In conclusion, among the materials tested herein, the highest CH_4 yield (CH_4 productivity) was observed for the bimetallic Ru0.2Ni20 DFM (20 wt% Ni and 0.2 wt% Ru) at 300 °C, with a value of 0.53 mmol g^{-1}, while the monometallic Ni20 DFM (20 wt% Ni) produced 0.45 mmol g^{-1} at the same temperature. The CO_2 adsorption capacity for both of these materials was similar, at 0.71 mmol g^{-1} at 300 °C. In order to facilitate good comparison with other recent literature works with similar material formulations, operating at a similar temperature range, a comparison table was prepared, which can be found at the Supplementary Material (Table S5). In light of this information, our materials indeed appear to present a quite good performance for ICCU-Methanation, and they compare favorably with those reported in the recent literature, both regarding the CH_4 yield/productivity and the CO_2 adsorption capacity, especially when considering the very low precious metal (Ru) loading for the bimetallic Ru-Ni DFM (Ru0.2Ni20) and the relatively low operation temperature (300 °C).

3.2.3. CO_2 methanation catalytic activity and kinetic study

Additionally, the CO_2 methanation catalytic activity and the respective reaction kinetics of the monometallic Ni20 DFM and the bimetallic Ru0.2Ni20 (0.2 wt% Ru) and Ru1Ni20 (1 wt% Ru) DFMs were studied under typical continuous-flow reaction conditions (Fig. 11). It is shown that upon the introduction of Ru, even at 0.2 wt% (Ru0.2Ni20), the CH_4 formation rate (in mol g_{cat}^{-1} s^{-1}) is substantially increased compared to the monometallic Ni20 DFM (Fig. 11a), whereas for the highest Ru loading of 1 wt% (Ru1Ni20), the CH_4 formation rate evidences a rather marginal further increase. The Ni-free, monometallic Ru0.2 reference material (0.2 wt% Ru in the absence of Ni) was also tested for comparison, showing a very low CH_4 formation rate, due to the much lower catalytically active metal content [52]. Additionally, the Arrhenius plots (Fig. 11b) allowed for the calculation of the activation energy for CH_4 production. This was calculated to be 93 kJ mol^{-1} for monometallic Ni20, 92 kJ mol^{-1} for bimetallic Ru0.2Ni20, and 95 kJ mol^{-1} for bimetallic Ru1Ni20 (all within the margin of error), meaning that the addition of Ru does not seem to significantly affect the activation energy [52].

The CO_2 and H_2 reaction orders were then calculated based on the plots of the logarithm of the CH_4 formation rate as a function of the logarithm of the CO_2 or H_2 partial pressure (in kPa), respectively (Fig. S10), according to Ref. [80]. The CO_2 order was calculated to be −0.23, −0.15, and −0.16 for Ni20, Ru0.2Ni20, and Ru1Ni20, respectively, whereas the H_2 order was calculated to be 1.30, 1.27, and 1.20 for Ni20, Ru0.2Ni20, and Ru1Ni20, respectively, which fall at a similar range to that of other relevant works [80,81]. The much higher values for the H_2 order compared to the negative values for the CO_2 order can be ascribed to the substantially increased CO_2 (or CO_2-derived species, e.g., carbonate) coverage in the presence of the "Na_2O" adsorption-active phase [80,81]. When comparing the different materials, the calculated H_2 order values are similar, whereas the CO_2 order values are slightly higher (in absolute values) for the Ru-containing materials, which can infer a certain effect of the Ru-phase on CO_2 activation.

3.2.4. In-situ DRIFTS investigation

Afterwards, the species present on the surface of the monometallic Ni20 and the bimetallic Ru0.2Ni20 DFMs during the individual steps of CO_2 adsorption, inert gas purge and methanation were investigated via in-situ DRIFTS, both at 300 and 400 °C operation (Fig. 12). Spectra were collected following the initiation of the CO_2 adsorption and methanation steps (ca. after 1 min), as well as at the end of the steps (i.e., after 15 min for adsorption, 5 min for purge, and 30 min for methanation). In all cases, the start of the adsorption period is characterized by the rapid formation of adsorbed carbonate species via the emergence of two large bands at approx. 1600 and 1350 cm^{-1}, which can be assigned to bidentate carbonates that are predominantly formed over the Al-O^--Na^+ adsorption-active sites [40,82,83]. The band at higher wavenumbers is accompanied by a quite small shoulder peak centered at approx. 1730–1770 cm^{-1}, which is more prevalent at the lower operating temperature of 300 °C, and, according to Merkouri et al. [83,84], it could be assigned to ionic carbonates. For the bimetallic Ru0.2Ni20 DFM, two smaller bands at approx. 2020 and 1920 cm^{-1} can be assigned to linear and bridged metal carbonyls (M−CO) [82–84]. The absence of these peaks for the monometallic Ni20 DFM indicates that these carbonyls are rather formed on Ru that is dispersed over the support and on the adjacent Ni sites. Indeed, the fact that Ru in Ru-Ni bimetallic materials can promote the dissociative adsorption of CO_2, and thus enhance the population of adsorbed CO intermediate species compared to monometallic Ni materials, has also been observed in other literature works [29,30,63–65]. At the higher wavenumber region (Fig. S11), the additional presence of bicarbonates can be observed via two bands at approx. 3740 and 3640 cm^{-1} [40]. During inert gas purge, most of the adsorbed species are retained, except for the weakly adsorbed bicarbonates, which are easily removed (Fig. S11).

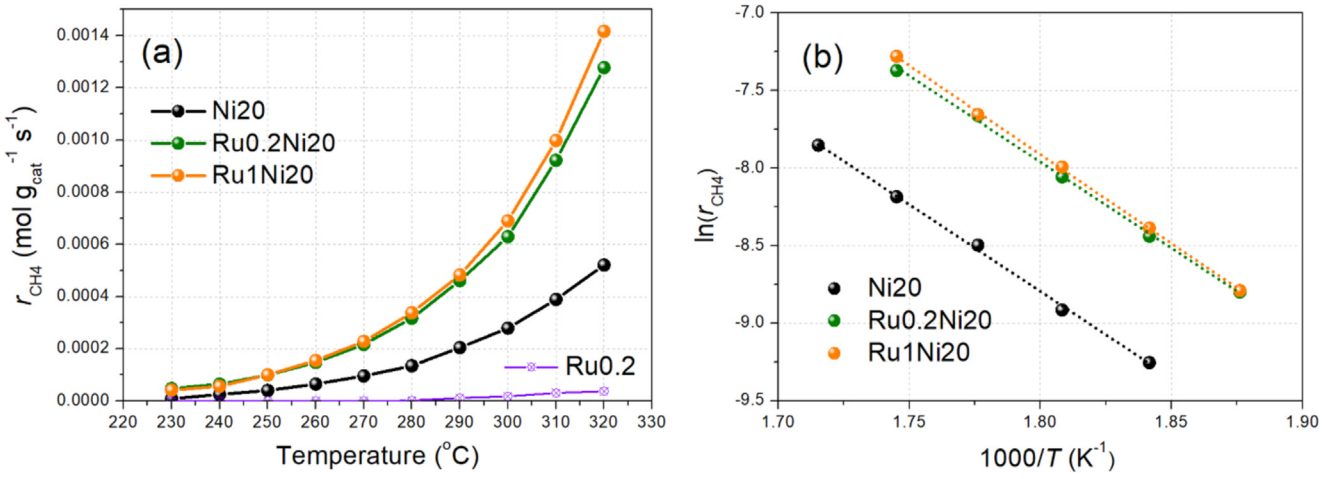

Fig. 11. (a) CH_4 formation rate as a function of reaction temperature and (b) natural logarithm of the CH_4 formation rate as a function of reciprocal temperature (Arrhenius plots).

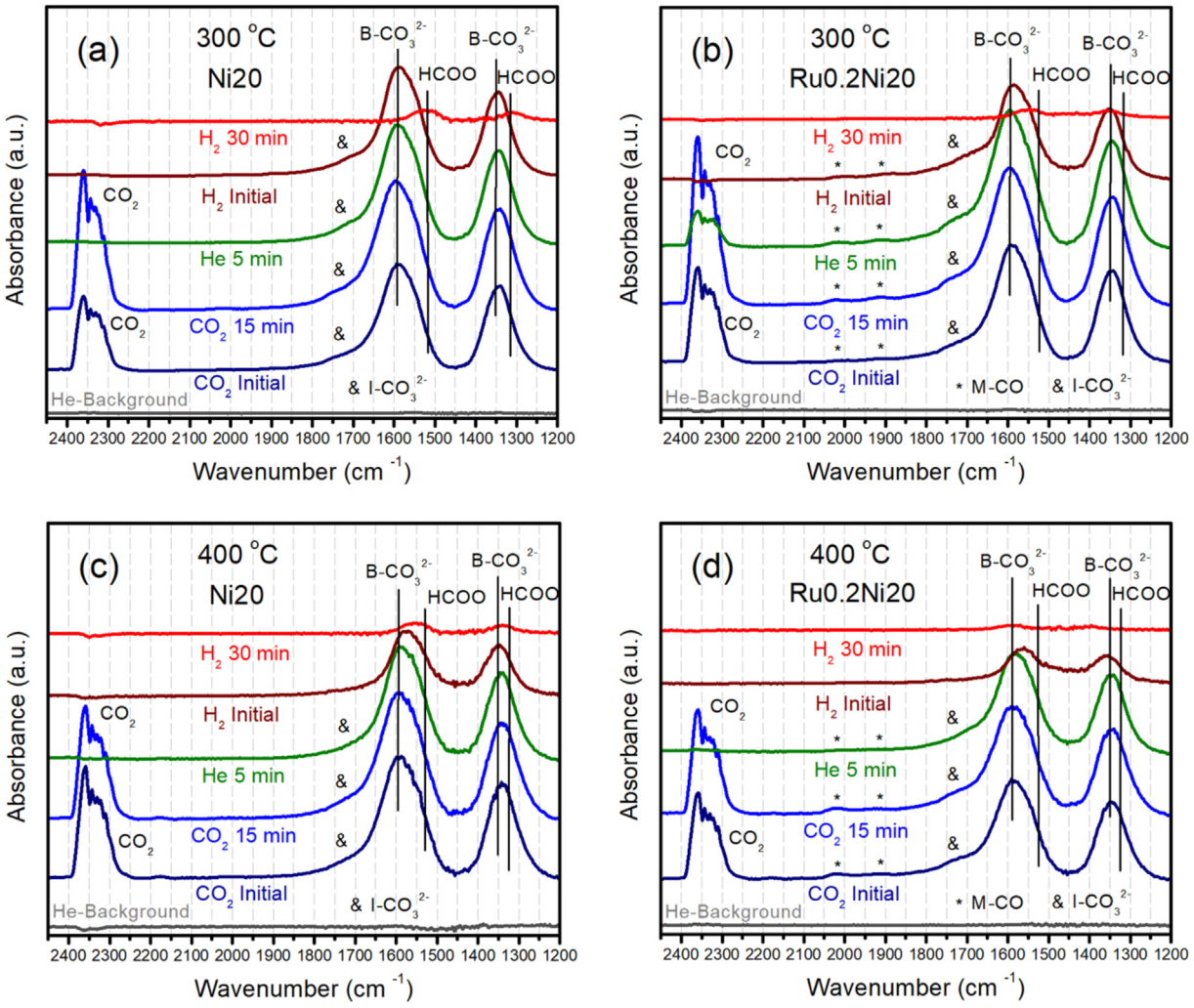

Fig. 12. In-situ DRIFTS spectra during the CO_2 adsorption step (initially and after 15 min), the purge step, and the hydrogenation step (initially and after 30 min), for the (a, c) Ni20 and (b, d) Ru0.2Ni20 DFMs at operating temperature of (a, b) 300 °C and (c, d) 400 °C. (B-CO_3^{2-}: Bidentate carbonates; HCOO: Formates; I-CO_3^{2-}: Ionic carbonates; M−CO: Metal carbonyls).

During the following hydrogenation step, the process of methanation for the pre-adsorbed carbonate species is initiated. At the onset of this step, the carbonate bands do not change to a significant degree, but the change is greater for the bimetallic Ru0.2Ni20 DFM and at the higher operating temperature of 400 °C. Also, the formation of gaseous CH_4 can be observed at higher wavenumbers (Fig. S11, insets) [40,85]. The intensity of the CH_4 peak in Fig. S11 is greater for the bimetallic Ru0.2Ni20 DFM, and in the case of the monometallic Ni20 DFM at the higher operating temperature of 400 °C, i.e., it is following the trend of the peak CH_4 concentration value during the ICCU-Methanation testing in Fig. 10. After 30 min of hydrogenation, the carbonate band intensity decreases and a shift toward lower wavenumbers is observed, which can be ascribed to the increased contribution of formate species [40,82,86]. As also evidenced in other works [40,82,86], the methanation of pre-adsorbed carbonates is suggested to proceed via their spillover to the metallic surface sites and through the formation of formate intermediate species (formate pathway). The weak signals peaking at approx. 2925 cm^{-1}, due to the C–H stretching vibrations of adsorbed formate species (Fig. S11, insets), also serve as further evidence for the existence of formate intermediate species [86]. The bands ascribed to the metal carbonyl species (Ru0.2Ni20) and ionic carbonates are removed following hydrogenation. The remaining (largely formate) bands after 30 min of hydrogenation have a lower intensity for the bimetallic Ru0.2Ni20 DFM. This is expected to be a result of the promoted methanation catalytic activity induced via the Ru presence, which facilitates a more rapid conversion for the reaction intermediates [82]. It should also be noted however, that the metal carbonyls (M−CO) over the bimetallic Ru0.2Ni20 DFM can also potentially act as active intermediates during the methanation reaction [29,30,63].

3.2.5. Material stability and effect of the oxidizing atmosphere during CO_2 adsorption

For the ICCU-Methanation process, it is also quite important to evaluate the material stability under successive adsorption-methanation cycles and also, with CO_2 capture performed under an oxidizing atmosphere (which causes the oxidation of the active metal phase). Since flue gases contain leftover O_2, the tolerance of DFMs during CO_2 capture under an oxidizing atmosphere is of particular importance, especially for Ni-based DFMs [8,14,20,87]. The stability testing consisted of 5 cycles under O_2-free CO_2 adsorption conditions (10% CO_2/Ar), followed by 5 cycles under O_2 presence during the adsorption of CO_2 (10% CO_2, 10% O_2 balance Ar), followed again by 5 cycles under 10% CO_2/Ar adsorption feed, with a similar protocol as to that applied in the works of Onrubia-Calvo et al. [88] and Boukha et al. [89].

Initially, the best-performing Ru0.2Ni20 DFM was tested at 300 °C (Fig. S12). The first 5 cycles with CO_2 adsorption under O_2-free conditions provided a stable CH_4 yield. When O_2 was introduced in the adsorption feed however, the CH_4 yield dropped sharply and continued to drop in subsequent cycles. Moreover, when the operation reverted back to adsorption under O_2-free conditions, the CH_4 yield was not recovered. This is attributed to the active metal phase oxidation under the oxidizing CO_2 capture conditions. The methanation-inactive NiO is not easily reduced back to metallic Ni at 300 °C (even in the presence of small Ru amounts), which therefore greatly limits the methanation catalytic activity [14].

We then proceeded to test the monometallic Ni20 and the bimetallic Ru0.2Ni20 DFMs at a higher operating temperature of 400 °C, in order to promote the material reduction following oxidation. Fig. 13 shows the CH_4 and CO yield values for all cycles, while Fig. S13 shows the CH_4 concentration profile and the cumulative CH_4 yield for the last cycle of each operation mode (CO_2 capture under either ideal or oxidizing conditions). During the first 5 cycles under ideal (O_2-free) CO_2 capture conditions (Cycles 1–5), both materials display a rather stable performance, with high CH_4 selectivity over CO and only a minor drop in the CH_4 yield values. When the operation mode changes to CO_2 capture under oxidizing conditions (Cycles 6–10), the total CH_4 yield for Ni20 becomes significantly lower (during the 6th cycle) and keeps reducing further for the subsequent cycles, down to 0.17 mmol g^{-1} during the 10th cycle. Moreover, the CH_4 production kinetics is also negatively impacted and CH_4 is produced quite slowly, with a broad signal (Fig. S13). As a result, NiO can only be partly reduced at 400 °C for Ni20 (in agreement with the XRD, H_2-TPR and XAS results), leading to a buildup of more oxidized NiO in subsequent cycles. For the bimetallic Ru0.2Ni20 DFM, the total CH_4 yield still drops under the oxidizing CO_2 capture atmosphere, but it remains relatively stable, with a value of 0.27 mmol g^{-1} during the 10th cycle. This value is approx. 52% higher when compared to the monometallic Ni20 DFM, which can be ascribed to the significantly higher reducibility and active metal ($NiO\text{-}RuO_x$) reduction degree at 400 °C upon just 0.2 wt% Ru addition (Table S1). The CO yield in this case is also much higher for the monometallic Ni20 DFM, and, as a result, CH_4 selectivity over CO stands at just around 70% for Ni20, compared to over 90% for Ru0.2Ni20. When we revert back to O_2-free operation (Cycles 11–15), the CH_4 yield is rapidly improved for Ru0.2Ni20 and then remains relatively stable, while monometallic Ni20 requires more cycles to recover its initial CH_4 yield, with its CH_4 selectivity over CO remaining at lower values than during Cycles 1–5.

Overall, it can be concluded that the presence of only a very small Ru loading in the DFM can significantly promote the ICCU-Methanation performance under both ideal and oxidizing CO_2 capture conditions. Both Ni20 and Ru0.2Ni20 DFMs can offer a high stability under an ideal CO_2 adsorption atmosphere, while sufficient activity and stability under an oxidizing CO_2 adsorption atmosphere are only observed for the bimetallic Ru-Ni DFM (with 0.2 wt% Ru).

Lastly, the potential cause for the drop in CH_4 yield (CH_4 productivity) during the subsequent cycles is investigated via transmission electron microscopy (HAADF-STEM along with EDS elemental mapping, Fig. S14). Although there is no evidence of coke deposition, a number of smaller-sized nanoparticles are observed to be sintered to a certain extent, forming some larger nanoparticles (>20 nm). Therefore, even though the majority of the smaller-sized Ni particles are retained, a small number of them is agglomerated/sintered, leading to a loss in the catalytically active surface area, and thus, in the CH_4 yield. For the spent bimetallic Ru0.2Ni20 DFM, sintering is observed for Ni as well, whereas Ru largely retains its originally high dispersion.

3.3. Process modelling results

3.3.1. Validation of the CFD model for different operating temperatures

The developed CFD model was initially validated for the monometallic Ni20 and the bimetallic Ru0.2Ni20 DFMs, as the operating temperature varied from 250 to 400 °C. Fig. 14 displays the comparison between the experimental and theoretical (CFD model) results regarding the CH_4 concentration evolution with time during the hydrogenation step, for both DFMs. It can be observed that the formation rate of CH_4 increases with the operating temperature. According to the Arrhenius equation, when the operating temperature is increased, the reaction rate constant, and herein the CH_4 formation rate, are also increased. The most pronounced difference regarding the formation rate of CH_4 is observed between the temperatures of 250 and 300 °C. The peak CH_4 concentration then reaches a maximum for both DFMs at 350 °C, and then, as the temperature is further increased to 400 °C, the reduced CO_2 adsorption capacity [13,41] hampers the total CH_4 production, and thus the maximum CH_4 concentration attainable during hydrogenation. The designed theoretical model was found to be in good agreement with the experimental results, showcasing the robustness of the developed CFD model and its ability in predicting the production of CH_4 during the ICCU-Methanation process. However, a significantly higher deviation was observed for lower operating temperatures (especially at

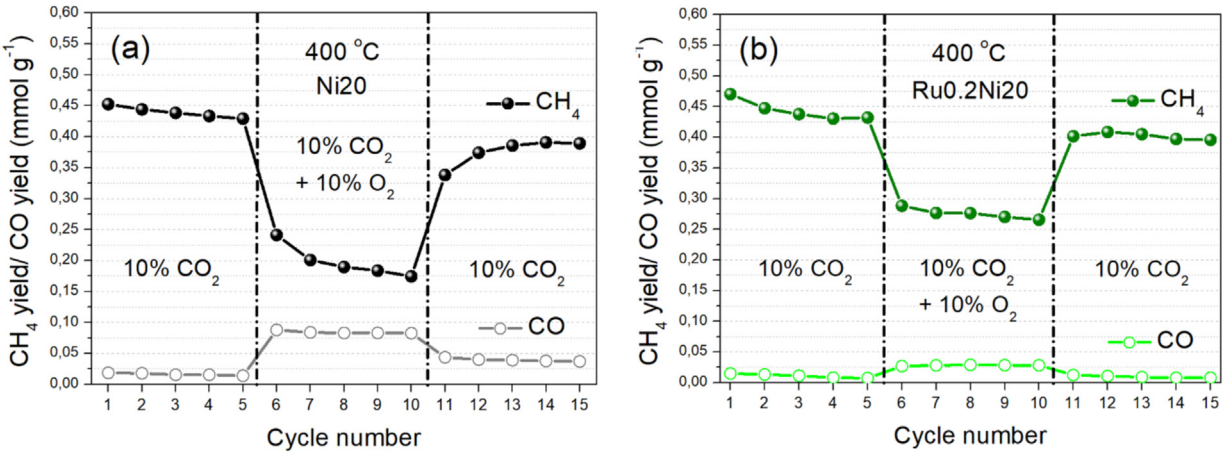

Fig. 13. CH_4 yield and CO yield for the (a) Ni20 and (b) Ru0.2Ni20 DFMs during successive adsorption-methanation cycles at 400 °C under both ideal and oxidizing CO_2 capture conditions.

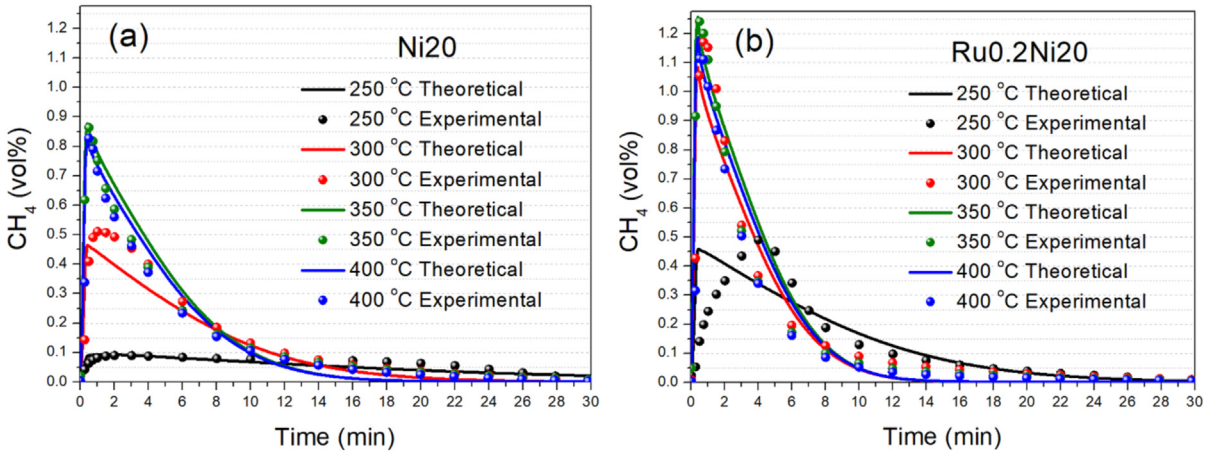

Fig. 14. Comparison between the experimental results and the CFD model (theoretical) results. Concentration of CH_4 at the reactor outlet as a function of reaction time during the hydrogenation step for the (a) Ni20 and (b) Ru0.2Ni20 DFMs at different operating temperatures. H_2 concentration = 10 vol%, inlet flow rate = 50 mL min^{-1}, DFM weight = 0.2 g, and reactor internal diameter = 0.9 cm.

250 °C), whereas the model was rather more effective in predicting the ICCU-Methanation performance at higher operating temperatures. Furthermore, the CFD model was also applied for the bimetallic Ru1Ni20 DFM with the highest Ru loading of 1 wt% at 300 and 400 °C (Fig. S15). For this material, the theoretical (computational) results were also found to be in good agreement with the experimental ones.

3.3.2. Prediction of the effect of different parameters on CH_4 formation

The CFD model was then applied in order to predict the effect of different operational parameters on the ICCU-Methanation process, for the best-performing bimetallic Ru0.2Ni20 DFM. The operating temperature in all these cases was set at 350 °C. First, the inlet H_2 concentration in the packed bed reactor was investigated from 5 vol% up to 20 vol%, with 10 vol% being the inlet H_2 concentration used in the initial study. The results demonstrated that CH_4 production is substantially increased for a higher H_2 inlet concentration (Fig. 15a). This can be ascribed to the fact that a higher H_2 partial pressure can lead to a higher surface coverage with H-species, which can in turn react with pre-adsorbed CO_2 [79,90]. It is also observed that the CH_4 concentration peaks become sharper with the rise of the inlet H_2 concentration, meaning that a higher inlet H_2 concentration can also benefit the CH_4 production kinetics. The theoretically obtained cumulative CH_4 yield is presented in Fig. S16a, showing that a higher inlet H_2 concentration can accelerate the CH_4 production and lead to an overall higher CH_4 productivity. This agrees with the experimental results of Porta et al. [91], who assessed the effect of the H_2 partial pressure on the hydrogenation step by varying the inlet H_2 concentration from 0.4 to 4 vol% H_2 (balance He), and observed an increase in the CH_4 yield and the peak CH_4 concentration by increasing the inlet H_2 concentration in the hydrogenation feed gas.

Afterwards, the effect of the inlet flow rate was examined. Four different inlet flow rates (25, 50, 100, and 200 mL min^{-1}) were investigated, with 50 mL min^{-1} being the inlet flow rate used in the initial study. From Fig. 15b, it can be observed that at lower inlet flow rates, and thus at lower flow to weight (F/W) ratios, higher CH_4 concentrations are obtained. This is attributed to the fact that at lower flow rates, the velocity of the fluid inside the reactor is decreased, and thus it takes longer for the fluid to exit the reactor (higher residence time), leading in turn to higher concentrations of the reaction product, i.e., CH_4, at the reactor effluent. Additionally, the cumulative CH_4 yield is displayed in Fig. S16b. The total CH_4 yield is actually higher for an inlet flow rate of 50 mL min^{-1}, compared to 25 mL min^{-1}. On the contrary, upon increasing the inlet flow rate to 100 and 200 mL min^{-1}, a reduction in the cumulative CH_4 yield can be observed. As such, an apparent maximum for the CH_4 yield is reached for a flow rate of 50 mL min^{-1} (F/W = 250 mL min^{-1} g^{-1}). According to Zheng et al. [92], CH_4 production during ICCU-Methanation can reach a maximum at moderate inlet flow rate values during hydrogenation, where a sufficient residence time is provided. Increasing the inlet flow rate beyond that point can cause a decrease in the CH_4 production, due to the decreased residence time that affects the kinetically limited reaction rate of the methanation of pre-adsorbed CO_2.

The DFM weight was another parameter that was investigated herein. By varying the mass of the material, the reactor bed porosity can be affected, since a higher material amount can decrease the free volume inside the reactor, and therefore the porosity of the packed bed. Four different DFM weight values were examined in this study, 0.05, 0.1, 0.2, and 0.4 g, with the 0.2 g value being the DFM weight used in the initial study. Fig. 15c shows the evolution of CH_4 with respect to hydrogenation time. As observed, higher CH_4 concentrations are obtained by increasing the mass of the DFM, and thus at lower flow to weight (F/W) ratios, since more adsorption and catalytically active sites exist in the reactor to perform the ICCU-Methanation process [22,25]. As for the cumulative CH_4 yield per gram of DFM (Fig. S16c), again, a maximum value is reached for 0.1–0.2 g of material (F/W = 250–500 mL min^{-1} g^{-1}). In the case of a lower amount of 0.05 g of material, a lower CH_4 yield is obtained, as the reactor's void volume is larger when compared to the other cases, and since, as previously mentioned, the space velocity and the residence time for the kinetically limited reaction are affected [92]. In the case of a higher amount of 0.4 g of material, the CH_4 yield is also lower, since the permeability of the reactor is influenced, and this can affect the ICCU-Methanation performance. The variation of the flow to weight (F/W) ratio was also investigated by Amin et al. [93], who showed that its effect on the catalytic activity is rather complex, with maximum catalytic activity being reached for an intermediate F/W value.

Lastly, the internal diameter of the reactor was varied. Four different values for the reactor internal diameter were examined (0.5, 0.7, 0.9, and 1.1 cm), with 0.9 cm being the reactor internal diameter used in the initial study. The bed porosity was the only parameter varied, while the material weight and the flow rate were kept constant at 0.2 g and 50 mL min^{-1}, respectively. The variation of the reactor internal diameter can influence the void volume of the packed bed reactor, since a lower reactor internal diameter

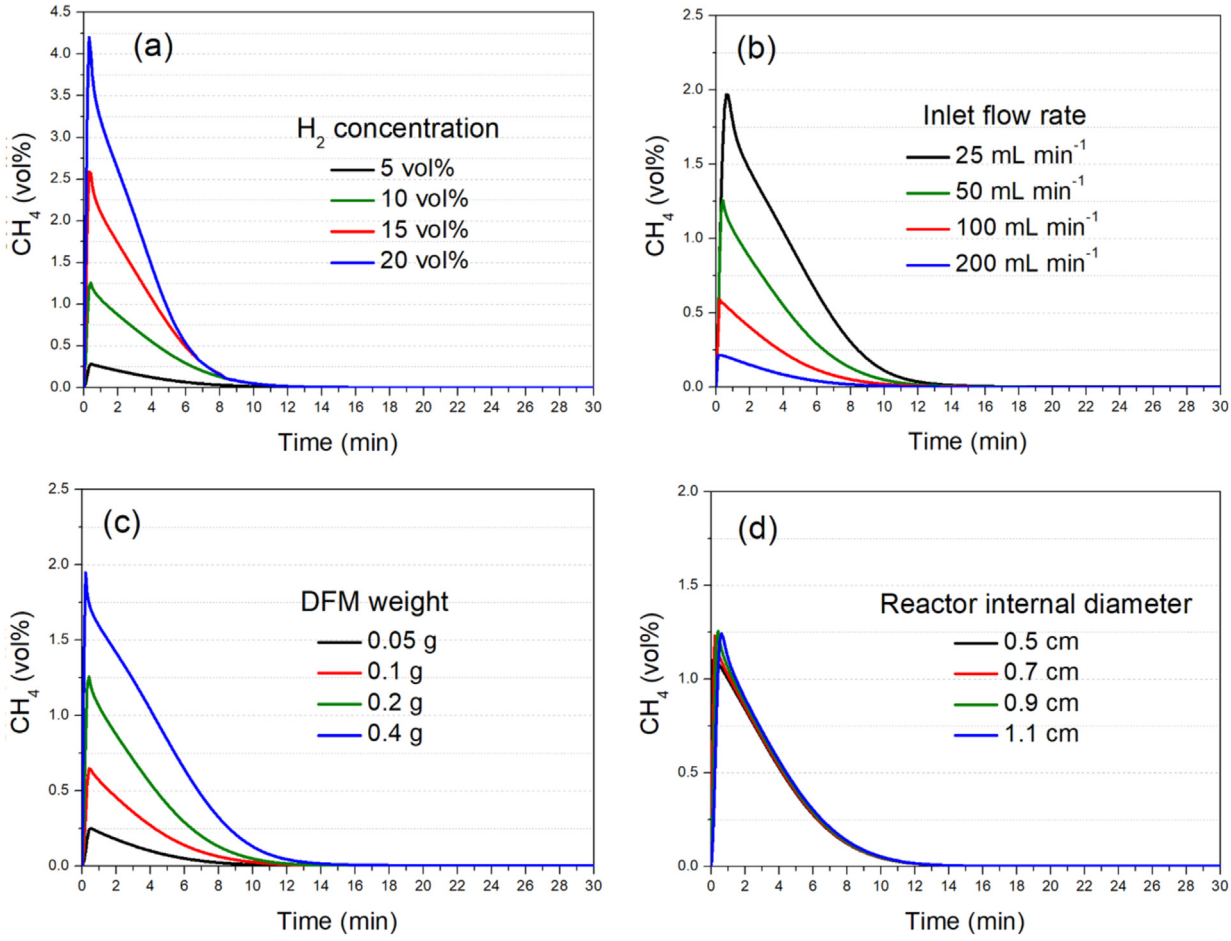

Fig. 15. Prediction of the effect of the (a) H_2 concentration, (b) inlet flow rate, (c) DFM weight, and (d) reactor internal diameter on the concentration of CH_4 at the reactor outlet as a function of reaction time during the hydrogenation step for the bimetallic Ru0.2Ni20 DFM. Temperature = 350 °C (a–d), H_2 concentration = 10 vol% (b–d), inlet flow rate = 50 mL min^{-1} (a, c, d), DFM weight = 0.2 g (a, b, d), and reactor internal diameter = 0.9 cm (a–c).

can lead to a drop in the void volume along with a rise in the fluid velocity, and vice versa [94]. The results did not show any significant differences in terms of the CH_4 concentration signal evolution (Fig. 15d) and the cumulative CH_4 yield (Fig. S16d). In a previous study [95], coating layers with a different thickness were investigated during CO_2 methanation in a coated wall reactor, with the catalyst mass being constant. The model predicted a small improvement in the CO_2 conversion values for less thick bed layers, with the difference between the results being however less than 10%. This might be due to the fact that the effects of the fluid velocity and bed porosity/void volume variation can be counterbalanced [96].

4. Conclusions

In this work, different bimetallic dual-function material (DFM) formulations were prepared with Ni as the main active metal phase and Ru as the secondary active metal phase supported on Na_2O/Al_2O_3, by varying the Ru:Ni bimetallic composition. It was shown that the active metal reducibility was drastically improved upon the addition of Ru even in very low loadings (0.1–0.2 wt%). As a result, the active metallic surface area could be significantly enhanced, leading to an increase in the population of surface-exposed catalytically active sites. Ni was found to form small and medium-sized nanoparticles. Ru on the other hand was highly dispersed as single atoms/small clusters, both on the support, as well as on the Ni particles (e.g., as single atom alloy sites), while also forming some rather small, segregated Ru particles, especially at higher Ru loadings.

Thereafter, it was shown that the bimetallic Ru-Ni DFMs with very low Ru loadings could demonstrate a significant enhancement in the ICCU-Methanation performance (CH_4 yield and CH_4 production kinetics) compared to the monometallic Ni-based DFM, with just 0.2 wt% Ru providing the best results. The main benefit regarding the CH_4 yield was observed at lower operating temperatures (250 and 300 °C), but the CH_4 production kinetics could be improved even at 400 °C. The ICCU-Methanation process was found to mainly proceed through CO_2 adsorption as rather bidentate carbonates, and then methanation via spillover to the metallic surface sites and the formation of formate intermediates. Moreover, the bimetallic Ru0.2Ni20 DFM (0.2 wt% Ru and 20 wt% Ni) displayed a high catalytic stability and a relatively good resistance toward CO_2 capture under an oxidizing atmosphere, significantly overperforming the monometallic Ni20 DFM.

The ICCU-Methanation performance at different operating temperatures could also be predicted via CFD modelling, with the experimental and theoretical results showing a relatively good agreement. The developed model was then applied in order to predict the effect of other operational parameters, including the inlet H_2 concentration, inlet flow rate, DFM weight, and reactor internal diameter. It was shown that a higher inlet H_2 concentration, a lower inlet flow rate, and a higher DFM weight (i.e., lower flow to weight ratio, F/W) could lead to a higher CH_4 concentration at the reactor outlet. On the other hand, the overall CH_4 productivity

was also favored with an increased inlet H_2 concentration, but could reach a maximum for an intermediate flow rate value of 50 mL min^{-1} and for a DFM weight between 0.1–0.2 g. Lastly, the variation of the reactor internal diameter, with the other parameters being kept constant, could not significantly affect the CH_4 concentration profile, nor the overall CH_4 yield.

In short, this work demonstrates the ability to substantially improve the ICCU-Methanation performance (CH_4 yield, CH_4 production kinetics, and resistance toward an oxidizing CO_2 capture atmosphere) of Ni-based DFMs via the addition of very low Ru loadings in the 0.1–0.2 wt% range, as well as the benefits of CFD modelling for predicting the ICCU-Methanation performance of DFMs and for performing parametric optimization.

CRediT authorship contribution statement

Anastasios I. Tsiotsias: Writing – original draft, Validation, Methodology, Investigation, Funding acquisition, Formal analysis, Data curation, Conceptualization. **Eleana Harkou:** Writing – original draft, Validation, Methodology, Investigation, Formal analysis, Data curation. **Nikolaos D. Charisiou:** Writing – review & editing, Supervision, Project administration, Formal analysis, Data curation, Conceptualization. **Victor Sebastian:** Writing – review & editing, Resources, Methodology, Investigation, Formal analysis, Data curation. **Dhanaji R. Naikwadi:** Methodology, Investigation, Formal analysis, Data curation. **Bart van der Linden:** Methodology, Investigation, Formal analysis, Data curation. **Atul Bansode:** Writing – review & editing, Validation, Resources. **Dragos Stoian:** Data curation, Formal analysis, Investigation, Methodology, Resources, Writing – review & editing, Validation. **George Manos:** Writing – review & editing, Validation, Resources. **Achilleas Constantinou:** Writing – review & editing, Validation, Resources. **Maria A. Goula:** Writing – review & editing, Supervision, Resources, Project administration, Funding acquisition, Conceptualization.

Declaration of competing interest

The authors declare that they have no known competing financial interests or personal relationships that could have appeared to influence the work reported in this paper.

Acknowledgments

NDC and MAG acknowledge support of this work by the project "Development of new innovative low carbon energy technologies to improve excellence in the Region of Western Macedonia" (MIS 5047197), which is implemented under the Action "Reinforcement of the Research and Innovation Infrastructure" funded by the Operational Program "Competitiveness, Entrepreneurship and Innovation" (NSRF 2014–2020) and co-financed by Greece and the European Union (European Regional Development Fund). AIT thanks the Hellenic Foundation for Research and Innovation (HFRI) for supporting this research work under the 3rd Call for HFRI PhD Fellowships (Fellowship Number: 6033). VS acknowledges the support of ELECMI-LMA node and Nanbiosis ICTSs. The BM31 setup was funded by the Swiss National Science Foundation (Grant: 206021_189629) and the Research Council of Norway (Grant: 296087).

Appendix A. Supplementary material

Supplementary data to this article can be found online at https://doi.org/10.1016/j.jechem.2024.11.001.

References

[1] W. Gao, S. Liang, R. Wang, Q. Jiang, Y. Zhang, Q. Zheng, B. Xie, C.Y. Toe, X. Zhu, J. Wang, L. Huang, Y. Gao, Z. Wang, C. Jo, Q. Wang, L. Wang, Y. Liu, B. Louis, J. Scott, A.C. Roger, R. Amal, H. He, S.E. Park, Chem. Soc. Rev. 49 (2020) 8584–8686.
[2] A.I. Latsiou, N.D. Charisiou, Z. Frontistis, A. Bansode, M.A. Goula, Catal. Today 420 (2023) 114179.
[3] D. Hidalgo, J.M. Martín-Marroquín, Renew. Sustain. Energy Rev. 132 (2020) 110057.
[4] G.I. Siakavelas, N.D. Charisiou, S. AlKhoori, A.A. AlKhoori, V. Sebastian, S.J. Hinder, M.A. Baker, I.V. Yentekakis, K. Polychronopoulou, M.A. Goula, Appl. Catal. B Environ. 282 (2021) 119562.
[5] J. Ren, H. Lou, N. Xu, F. Zeng, G. Pei, Z. Wang, J. Energy Chem. 80 (2023) 182–206.
[6] J. Ren, F. Zeng, C. Mebrahtu, Z. Wang, R. Palkovits, J. Energy Chem. 86 (2023) 351–361.
[7] Z. Lv, S. Chen, X. Huang, C. Qin, Curr. Opin. Green Sustain. Chem. 40 (2023) 100771.
[8] M. Abdallah, R. Farrauto, Catal. Today 423 (2023) 113923.
[9] L.P. Merkouri, T.R. Reina, M.S. Duyar, Energy and Fuels 35 (2021) 19859–19880.
[10] A.I. Tsiotsias, N.D. Charisiou, I.V. Yentekakis, M.A. Goula, Catalysts 10 (2020) 812.
[11] J. Chen, Y. Xu, P. Liao, H. Wang, H. Zhou, Carbon Capture Sci. Technol. 4 (2022) 100052.
[12] B. Shao, Y. Zhang, Z. Sun, J. Li, Z. Gao, Z. Xie, J. Hu, H. Liu, Green Chem. Eng. 3 (2022) 189–198.
[13] A.I. Tsiotsias, N.D. Charisiou, A.G.S. Hussien, A.A. Dabbawala, V. Sebastian, K. Polychronopoulou, M.A. Goula, J. Environ. Chem. Eng. 12 (2024) 112712.
[14] M.A. Arellano-Treviño, Z. He, M.C. Libby, R.J. Farrauto, J. CO_2 Util. 31 (2019) 143–151.
[15] A. Bermejo-López, B. Pereda-Ayo, J.A. González-Marcos, J.R. González-Velasco, Appl. Catal. B Environ. 256 (2019) 117845.
[16] S. Wang, E.T. Schrunk, H. Mahajan, R.J. Farrauto, Catalysts 7 (2017) 88.
[17] A.C. Faria, R. Trujillano, V. Rives, C.V. Miguel, A.E. Rodrigues, L.M. Madeira, J. CO_2 Util. 72 (2023) 102476.
[18] E. García-Bordejé, A. Belén Dongil, J.M. Conesa, A. Guerrero-Ruiz, I. Rodríguez-Ramos, Chem. Eng. J. 472 (2023) 144953.
[19] Z. Guo, S. Gao, S. Xiang, J. Wang, G. Mao, H. Jiang, X. Dong, Y. Teng, Chem. Eng. J. 481 (2024) 148599.
[20] M.A. Arellano-Treviño, N. Kanani, C.W. Jeong-Potter, R.J. Farrauto, Chem. Eng. J. 375 (2019) 121953.
[21] A. Bermejo-López, B. Pereda-Ayo, J.A. Onrubia-Calvo, J.A. González-Marcos, J.R. González-Velasco, J. Environ. Chem. Eng. 11 (2023) 109401.
[22] A.I. Tsiotsias, N.D. Charisiou, E. Harkou, S. Hafeez, G. Manos, A. Constantinou, A. G.S. Hussien, A.A. Dabbawala, V. Sebastian, S.J. Hinder, M.A. Baker, K. Polychronopoulou, M.A. Goula, Appl. Catal. B Environ. 318 (2022) 121836.
[23] S. Hafeez, S.M. Al-Salem, K.N. Papageridis, N.D. Charisiou, M.A. Goula, G. Manos, A. Constantinou, Catalysts 11 (2021) 747.
[24] A.I. Tsiotsias, S. Hafeez, N.D. Charisiou, S.M. Al-Salem, G. Manos, A. Constantinou, S. AlKhoori, V. Sebastian, S.J. Hinder, M.A. Baker, K. Polychronopoulou, M.A. Goula, Renew. Energy 206 (2023) 582–596.
[25] A. Bermejo-López, B. Pereda-Ayo, J.A. González-Marcos, J.R. González-Velasco, J. CO_2 Util. 42 (2020) 101351.
[26] A. Bermejo-López, B. Pereda-Ayo, J.A. González-Marcos, J.R. González-Velasco, Catal. Today 394–396 (2022) 314–324.
[27] J. Hu, F. Yang, J. Qu, Y. Cai, X. Yang, C.M. Li, J. Energy Chem. 87 (2023) 162–191.
[28] A.I. Tsiotsias, N.D. Charisiou, I.V. Yentekakis, M.A. Goula, Nanomaterials 11 (2021) 28.
[29] A. Quindimil, M.C. Bacariza, J.A. González-Marcos, C. Henriques, J.R. González-Velasco, Appl. Catal. B Environ. 296 (2021) 120322.
[30] Y. Pan, X. Han, X. Chang, H. Zhang, X. Zi, Z. Hao, J. Chen, Z. Lin, M. Li, X. Ma, Ind. Eng. Chem. Res. 62 (2023) 4344–4355.
[31] L.M.N.C. Alves, M.P. Almeida, M. Ayala, C.D. Watson, G. Jacobs, R.C. Rabelo-Neto, F.B. Noronha, L.V. Mattos, Chem. Eng. Sci. 239 (2021) 116604.
[32] M. Thommes, K. Kaneko, A.V. Neimark, J.P. Olivier, F. Rodriguez-Reinoso, J. Rouquerol, K.S.W. Sing, Pure Appl. Chem. 87 (2015) 1051–1069.
[33] B. Ravel, M. Newville, J. Synchrotron Rad. 12 (2005) 537–541.
[34] A.I. Tsiotsias, N.D. Charisiou, A. AlKhoori, S. Gaber, V. Stolojan, V. Sebastian, B. van der Linden, A. Bansode, S.J. Hinder, M.A. Baker, K. Polychronopoulou, M.A. Goula, J. Energy Chem. 71 (2022) 547–561.
[35] L. Falbo, M. Martinelli, C.G. Visconti, L. Lietti, C. Bassano, P. Deiana, Appl. Catal. B Environ. 225 (2018) 354–363.
[36] J.F. Richardson, J.H. Harker, J.R. Backhurst, in: Chemical Engineering, fifth ed., Vol. 2, Elsevier, 2022, pp. 191–236.
[37] H. S. Fogler, Elements of Chemical Reaction Engineering. sixth ed., Pearson, London, 2020.
[38] N. Froessling, Gerlands Beiträge Zur Geophysik, Vol. 52, No. 1, 1938.
[39] C.J. Keturakis, F. Ni, M. Spicer, M.G. Beaver, H.S. Caram, I.E. Wachs, ChemSusChem 7 (2014) 3459–3466.
[40] L. Proaño, E. Tello, M.A. Arellano-Trevino, S. Wang, R.J. Farrauto, M. Cobo, Appl. Surf. Sci. 479 (2019) 25–30.
[41] A.I. Tsiotsias, A.G. Georgiadis, N.D. Charisiou, A.G.S. Hussien, A.A. Dabbawala, K. Polychronopoulou, M.A. Goula, ACS Omega 9 (2024) 11305–11320.

[42] Z. Zhang, Y. Tian, L. Zhang, S. Hu, J. Xiang, Y. Wang, L. Xu, Q. Liu, S. Zhang, X. Hu, Int. J. Hydrogen Energy 44 (2019) 9291–9306.
[43] D. Beierlein, D. Häussermann, M. Pfeifer, T. Schwarz, K. Stöwe, Y. Traa, E. Klemm, Appl. Catal. B Environ. 247 (2019) 200–219.
[44] N.D. Charisiou, G. Siakavelas, K.N. Papageridis, A. Baklavaridis, L. Tzounis, K. Polychronopoulou, M.A. Goula, Int. J. Hydrogen Energy 42 (2017) 13039–13060.
[45] A. Bermejo-López, B. Pereda-Ayo, J.A. González-Marcos, J.R. González-Velasco, Sustain. Energy Fuels 5 (2021) 1194–1210.
[46] L. Zhou, L. Li, N. Wei, J. Li, J.M. Basset, ChemCatChem 7 (2015) 2508–2516.
[47] A.G. Georgiadis, A.I. Tsiotsias, G.I. Siakavelas, N.D. Charisiou, B. Ehrhardt, W. Wang, V. Sebastian, S.J. Hinder, M.A. Baker, S. Mascotto, M.A. Goula, Renew. Energy 227 (2024) 120511.
[48] C. Jeong-Potter, M. Abdallah, S. Kota, R. Farrauto, Ind. Eng. Chem. Res. 61 (2022) 10474–10482.
[49] A. Bermejo-López, B. Pereda-Ayo, J.A. González-Marcos, J.R. González-Velasco, J. CO_2 Util. 34 (2019) 576–587.
[50] B. Rudolph, A.I. Tsiotsias, B. Ehrhardt, P. Dolcet, S. Gross, S. Haas, N.D. Charisou, M.A. Goula, S. Mascotto, Adv. Sci. 10 (2023) 2205890.
[51] A.G. Georgiadis, G.I. Siakavelas, A.I. Tsiotsias, N.D. Charisiou, B. Ehrhardt, W. Wang, V. Sebastian, S.J. Hinder, M.A. Baker, S. Mascotto, M.A. Goula, Int. J. Hydrogen Energy 48 (2023) 19953–19971.
[52] A.I. Tsiotsias, N.D. Charisiou, C. Italiano, G.D. Ferrante, L. Pino, A. Vita, V. Sebastian, S.J. Hinder, M.A. Baker, A. Sharan, N. Singh, K. Polychronopoulou, M. A. Goula, Appl. Surf. Sci. 646 (2024) 158945.
[53] Z. Luo, Z. Zheng, L. Li, Y.T. Cui, C. Zhao, ACS Catal. 7 (2017) 8304–8313.
[54] A. Porta, C.G. Visconti, L. Castoldi, R. Matarrese, C. Jeong-Potter, R. Farrauto, L. Lietti, Appl. Catal. B Environ. 283 (2021) 119654.
[55] S. Velu, S.K. Gangwal, Solid State Ionics 177 (2006) 803–811.
[56] Y. Du, C. Qin, Y. Xu, D. Xu, J. Bai, G. Ma, M. Ding, Chem. Eng. J. 418 (2021) 129402.
[57] A.I. Tsiotsias, N.D. Charisiou, A. Alkhoori, S. Gaber, V. Sebastian, S.J. Hinder, M. A. Baker, K. Polychronopoulou, M.A. Goula, J. CO_2 Util. 61 (2022) 102046.
[58] Y. Zhou, A. Sadia Traore, D.V. Peron, A.J. Barrios, S.A. Chernyak, M. Corda, O.V. Safonova, A. Iulian Dugulan, O. Ersen, M. Virginie, V.V. Ordomsky, A.Y. Khodakov, J. Energy Chem. 85 (2023) 291–300.
[59] T. Sasayama, F. Kosaka, Y. Liu, T. Yamaguchi, S.Y. Chen, T. Mochizuki, A. Urakawa, K. Kuramoto, J. CO_2 Util. 60 (2022) 102049.
[60] D. Pinto, S. Minorello, Z. Zhou, A. Urakawa, J. Environ. Sci. 140 (2024) 113–122.
[61] A. Bustinza, M. Frías, Y. Liu, E. García-Bordejé, Catal. Sci. Technol. 10 (2020) 4061–4071.
[62] T.A. Le, J. Kim, J.K. Kang, E.D. Park, Catal. Today 356 (2020) 622–630.
[63] T. Zhang, P. Zheng, F. Gu, W. Xu, W. Chen, T. Zhu, Y.F. Han, G. Xu, Z. Zhong, F. Su, Appl. Catal. B Environ. 323 (2023) 122190.
[64] T. Zhang, P. Zheng, J. Gao, Z. Han, F. Gu, W. Xu, L. Li, T. Zhu, Z. Zhong, G. Xu, F. Su, Small 20 (2023) 2308193.
[65] W. Liu, H. Feng, Y. Yang, Y. Niu, L. Wang, P. Yin, S. Hong, B. Zhang, X. Zhang, M. Wei, Nat. Commun. 13 (2022) 3188.
[66] K.N. Papageridis, N.D. Charisiou, S. Douvartzides, V. Sebastian, S.J. Hinder, M.A. Baker, S. AlKhoori, K. Polychronopoulou, M.A. Goula, Renew. Energy 162 (2020) 1793–1810.
[67] N.D. Charisiou, K.N. Papageridis, L. Tzounis, V. Sebastian, S.J. Hinder, M.A. Baker, M. AlKetbi, K. Polychronopoulou, M.A. Goula, Int. J. Hydrogen Energy 44 (2019) 256–273.
[68] J.R. Deka, D. Saikia, K.-S. Hsia, H.-M. Kao, Y.-C. Yang, C.-S. Chen, Catalysts 10 (2020) 267.
[69] K. Cui, W. Qian, Z. Shao, X. Zhao, H. Gong, X. Wei, J. Wang, M. Chen, Catal. Letters 151 (2021) 2513–2526.
[70] S. Chen, A.M. Abdel-Mageed, M. Dyballa, M. Parlinska-Wojtan, J. Bansmann, S. Pollastri, L. Olivi, G. Aquilanti, R.J. Behm, Angew. Chem. Int. Ed. 59 (2020) 22763–22770.
[71] V. Malinovschi, A.H. Marin, C. Ducu, S. Moga, V. Andrei, E. Coaca, V. Craciun, M. Lungu, C.P. Lungu, Coatings 12 (2022) 29.
[72] C.B. Soni, S.K. Sungjemmenla, V.K. Vineeth, Energy Storage 4 (2022) 264.
[73] A.I. Tsiotsias, B. Ehrhardt, B. Rudolph, L. Nodari, S. Kim, W. Jung, N.D. Charisiou, M.A. Goula, S. Mascotto, ACS Nano 16 (2022) 8904–8916.
[74] K. Khivantsev, N.R. Jaegers, H.A. Aleksandrov, I. Song, X.I. Pereira-Hernandez, M.H. Engelhard, J. Tian, L. Chen, D.M. Meira, L. Kovarik, G.N. Vayssilov, Y. Wang, J. Szanyi, J. Am. Chem. Soc. 145 (2023) 5029–5040.
[75] M.S. Duyar, M.A. Arellano-Treviño, R.J. Farrauto, Appl. Catal. B Environ. 168–169 (2015) 370–376.
[76] P. Huang, Y. Guo, G. Wang, J. Yu, C. Zhao, X. Wang, T. Wang, Energy and Fuels 35 (2021) 20185–20196.
[77] A.I. Tsiotsias, A.G. Georgiadis, N.D. Charisiou, M.A. Goula, Materials. 16 (2023) 6656.
[78] W.J. Lee, C. Li, H. Prajitno, J. Yoo, J. Patel, Y. Yang, S. Lim, Catal. Today 368 (2021) 2–19.
[79] A. Quindimil, J.A. Onrubia-Calvo, A. Davó-Quiñonero, A. Bermejo-López, E. Bailón-García, B. Pereda-Ayo, D. Lozano-Castelló, J.A. González-Marcos, A. Bueno-López, J.R. González-Velasco, J. CO_2 Util. 57 (2022) 101888.
[80] S.J. Park, M.P. Bukhovko, C.W. Jones, Chem. Eng. J. 420 (2021) 130369.
[81] S.J. Park, X. Wang, M.R. Ball, L. Proano, Z. Wu, C.W. Jones, Catal. Sci. Technol. 12 (2022) 4637.
[82] L. Proaño, M.A. Arellano-Treviño, R.J. Farrauto, M. Figueredo, C. Jeong-Potter, M. Cobo, Appl. Surf. Sci. 533 (2020) 147469.
[83] L.P. Merkouri, J.L. Martín-Espejo, L.F. Bobadilla, J.A. Odriozola, A. Penkova, T. Ramirez Reina, M.S. Duyar, J. Mater. Chem. A 11 (2023) 13209–13216.
[84] L.P. Merkouri, J.L. Martín-Espejo, L.F. Bobadilla, J.A. Odriozola, M.S. Duyar, T.R. Reina, Nanomaterials 13 (2023) 506.
[85] L. Truong-Phuoc, J.M. Nhut, L. Vidal, C. Duong-Viet, S. Sall, C. Petit, C. Sutter, M. Arab, A. Jourdan, C. Pham-Huu, J. Energy Chem. 85 (2023) 310–323.
[86] S. Cimino, E. Maria, F. Frusteri, L. Lisi, Sep. Purif. Technol. 354 (2025) 129101.
[87] J.A. Onrubia-Calvo, B. Pereda-Ayo, J.A. González-Marcos, J.R. González-Velasco, J. CO_2 Util. 81 (2024) 102704.
[88] J.A. Onrubia-Calvo, A. Bermejo-López, B. Pereda-Ayo, J.A. González-Marcos, J.R. González-Velasco, Appl. Catal. B Environ. 321 (2023) 122045.
[89] Z. Boukha, A. Bermejo-López, U. De-La-Torre, J.R. González-Velasco, Appl. Catal. B Environ. 338 (2023) 122989.
[90] M.A. Vasiliades, N.S. Govender, A. Govender, R. Crous, D. Moodley, T. Botha, A. M. Efstathiou, ACS Catal. 12 (2022) 15110–15129.
[91] A. Porta, R. Matarrese, C.G. Visconti, L. Lietti, Energy and Fuels 37 (2023) 7280–7290.
[92] Q. Zheng, R. Farrauto, A. Chau Nguyen, Ind. Eng. Chem. Res. 55 (2016) 6768–6776.
[93] N.A.S. Amin, S.E. Pheng, Chem. Eng. J. 116 (2006) 187–195.
[94] J. Pottbäcker, O. Hinrichsen, Chem. Ing. Tech. 89 (2017) 454–458.
[95] E. Harkou, S. Hafeez, P. Adamou, Z. Zhang, A.I. Tsiotsias, N.D. Charisiou, M.A. Goula, S.M. Al-Salem, G. Manos, A. Constantinou, Environ. Res. 236 (2023) 116760.
[96] G.S. Beavers, E.M. Sparrow, D.E. Rodenz, J. Appl. Mech. 40 (1973) 655–660.